UNIVERSITÀ DEGLI STUDI DI PARMA

Dottorato di Ricerca in Tecnologie dell'Informazione

XXVII Ciclo

FLEXIBLE LOW-LOSS THz AND ULTRA HIGH-POWER IR WAVEGUIDING USING PCFs

Coordinatore:

Chiar.mo Prof. Marco Locatelli

Tutor:

Chiar.mo Prof. Stefano Selleri

Dottorando: *Masruri Masruri*

Gennaio 2015

to my parents,
kiki, izzi, and zahra

Outline

List of Figures

List of Tables

Introduction

Special optical fibers known as Photonic Crystal Fibers (PCFs) have attracted considerable attention of research communities and industries for peculiar propagation characteristics and prove to have wide range of applications, such as security, sensing, high power fiber laser, and communications. PCFs can be designed to work in wide range of frequency range from lower frequency regions (visible to infrared wavelength range) to high frequency of THz region. The optical properties of materials in PCF can be controlled by proper design of the fiber cross-section to have waveguiding properties that are very different from those of the conventional optical fibers. The PCFs consist of an optical guiding central core surrounded by an ordered arrangement of air holes in the cladding region. The holes occur in a regular or periodic pattern or "crystal" that extends along the length of the fiber. PCFs with solid core exhibits index guiding in which the optical energy propagates through the core by total internal reflection in a manner similar to conventional step index optical fiber. PCFs with the hollow (air) core can exhibit two kinds of waveguiding mechanisms: photonic band-gap (PBG) and inhibited coupling (IC). PBG prevents the propagation of a certain wavelength in the cladding by proper design geometry to the microstructure. IC fibers guide via inhibited coupling (IC) between the cladding modes and the guided core modes. In this waveguiding mechanism the confinement relies on a strong reduction of the coupling between core modes and cladding modes. Inhibited coupling mechanism exhibits broader transmission bandwidth but with a relatively higher loss than photonic band-gap.

The design of complex Photonic Crystal Fibers requires the numerical analysis

to understand the light guiding mechanism, rather than an analytical one. Techniques from traditional fiber theory are inadequate due to the complex geometry of the PCFs. The Finite Element Method (FEM) is useful to provide the numerical solution which is suitable for the complexity of PCF structure. The basic idea of FEM is to split the 2D domain of electromagnetic problem, in this case it is represented by the optical cross-section, in a large number of triangular elements called by mesh. Over the mesh the differential electromagnetic problem can be discretized, locally linearized and finally solved.

Among wide area of PCF applications, the PhD activity mainly focus on two interesting applications of PCF: high power fiber laser in IR region and low-loss waveguiding in THz region. The applications will be presented in relation with the kind of PCF designs. Large Pitch PCF, short called by Large Pitch Fiber (LPF), a hexagonal PCF structure, enable the large mode area and achieves the delocalization property of higher order modes, granted high output power and good beam quality. The properties are maintained even by scaling the whole structure to obtain the large mode area. In the mid-infrared range of 2 μm - 3 μm, the double cladding silica based PCF with 80 μm-core and reduced cladding symmetry has been investigated, aiming to obtain robust single mode guiding even at high power load of fiber lasers. Single mode propagation with effective area larger than 2500 μm^2 has been demonstrated at heat load of 340 W/m. For THz region, the PCF obtained by arranging N dielectric tubes made by Zeonex plastic material in a circular pattern has been designed and optimized for flexible low-loss waveguiding of terahertz application. The fibers guide through inhibited coupling. Using the FEM, the scaling laws of confinement loss and absorption loss of the fibers have been numerically investigated with the purpose to obtain design guidelines for small and flexible low loss THz waveguides. By choosing the a total reference value of 10 dB/m, a remarkable transmission band of about an octave, ranging from 0.7 THz to 1.3 THz, is obtained with N = 16. By reducing the reference loss value as low as 1 dB/m the maximum band of 280 GHz is obtained with N = 14, ranging from 0.94 THz to 1.22 THz. The bandwidth can be further increased significantly in higher frequency range with lower minimum loss at the expense of the slightly loss of the bandwidth in lower frequency by reducing the tube thickness

and applying the touchless cladding tubes. Around one and half larger bandwidth is obtained for about 400 GHz range from 0.97 THz to 1.37 THz using this approach with $N = 14$ using the reference loss of 1 dB/m.

The doctoral thesis consists of the following outline. Chapter 1 will present a brief introduction of photonic crystal fiber, Chapter 2 presents Large Pitch Fiber (LPF) for their properties of delocalization of higher order modes which are useful for high power fiber lasers. Chapter 3 presents numerical analysis of Tm-doped DC-PCF using a full-vector modal solver based on the finite-element method with integrated thermal model to analysis the influence of thermal effect on the delocalization properties of the fiber. The design of Symmetry-Free cladding (SF-PCF) and a core diameter of 80 μm to achieve a single mode operation even in the high thermal load fiber laser will be investigated and compared with LPF one. Chapter 4 presents Circular Tube Lattice Fiber (CTLF). The chapter presents numerical analysis of scaling laws of the fiber losses with the purpose to obtain design guidelines for small and flexible low loss waveguides. Small fiber diameter of CTLF then will be presented for low-loss THz waveguiding. Conclusion and the synthesis of results will follow. In overall analysis of PCF types, a full-vector modal solver based on the finite-element method will be used.

Chapter 1

Photonic crystal fiber

Since the first development of photonic crystal fiber (PCF) by Philip Russel in the mid 1990s [5], PCFs have attracted a tremendous attention from research communities and industries for their peculiar characteristics. Unlike conventional optical fibers, which use different core and cladding materials, PCFs can be made from a single material by exploiting huge variety of air-holes arrangement that run along the fiber length. PCFs provide high degree of freedom in their cross-section design for controlling fiber properties such as different fiber structure, hole shape, hole size, the separation between the air-holes, the air-hole arrangement, and different fill. Modification of those parameters allows to obtain desirable optical properties such as endlessly single mode operation [6], tailorable dispersion [7], large optical nonlinearity [8], high birefringence [9], large mode area [10][11]. As such, PCFs offer a wide range of applications such as creating white light supercontinuum sources, polarization maintaining fibers, high-power fiber optics, fiber biosensing and medical applications. Great design flexibility of PCFs combined with large choice of single dielectric material beyond the silica, creates a wide possibility for PCFs to work in a wide range of frequency regions from lower frequencies (from visible and near-infrared telecommunication window, to mid and far-infrared region) and high frequency of THz region.

PCFs consist of solid-core PCFs and hollow-core PCFs. Solid core PCFs rely on

one of the following guidance mechanisms: a modified total internal reflection (index guiding), or photonic bandgap (PBG) guidance. The former mechanism is similar to the usual step-index fiber in which the refractive index of the core is larger than that of the cladding. Solid core photonic bandgap fibers consist of an array of high index circular rods embedded in a low index background. The spectral properties of such solid core PBG fibers can be described analytically by use of a so-called antiresonant reflecting optical waveguide (ARROW) model [12]. The fiber guides light in a low-index core if it is in antiresonance with the high-index inclusions (isolated circular rods) in which the light is reflected back into the core. In the case of resonance with the high-index inclusions the spectral regions have high confinement loss. It might be noted that the frequency positions of the transmission windows depend mostly on the index contrast and the diameter of the inclusions rather than the lattice constant.

Hollow core PCFs work in two types of waveguiding mechanism: photonic band gap (PBG) or inhibited coupling (IC). It must be noticed, however, that for both of these mechanisms the confinement of the electromagnetic radiation inside the core region is not perfect due to the loss which can be divided into two terms: absorption loss due to the dielectric materials used in the waveguide, and confinement loss due to the non perfect confinement of the electromagnetic radiation inside the core region that causes part of the power radiates out of the waveguide. PBG fibers work by exploiting the physics of photonic bandgaps (PBGs). These fibers consist of an optical-guiding central air-core surrounded by a lattice of hollow microchannels (a two-dimensional photonic crystal) running along its length. A periodic arrangement of the refractive index in the cladding in such a way can obtain a frequency dependent core-cladding reflection for the electromagnetic radiation that is confined inside the hollow core. PBGs offer very low loss around 1.2 dB/km at telecoms wavelengths [13] over restricted wavelength bands, e.g. 100-200 nm, which is useful in applications requiring long-distance transmission.

1.1 PCFs in infrared regions

Much amount of research works with PCFs has been concentrated on the near infrared (IR) telecommunication bands (around 1300 nm and 1550 nm). In these bands PCFs are usually made from silica fibers which can work from visible to IR. However, silica fibers start attenuating very heavily beyond $\sim$2 μm. It can be realizable that by using different core materials PCFs will be able to push the wavelength performance into the mid IR and beyond. Conventional fibers are available that can transmit beyond $\sim$2 μm. They use zirconium fluoride that can work from 0.45-5 μm, chalcogenide fibers from 2-11 μm and silver halide fibers from 4-18 μm, but these fibers have significant absorption features and more expensive than similar silica fibers.

The example of PCFs applications working in wideband operation from visible to near-infrared is endlessly single-mode photonic crystal fibers [6]. The fibers are undoped silica fibers that use a triangular pattern of air holes to form the cladding. Since the index contrast between the core and the cladding, Δn, is determined only by the geometry of the air holes, it is possible to fabricate fibers with a very small and accurate Δn, and thus obtain very low numerical apertures and the effective normalized frequency can be kept below 2.405 (single-mode regime). Furthermore, this type of fiber is single-mode over a very broad wavelength range, starting from recommended wavelength of around $\sim$450 nm to 1550 at least. The fibers use smaller holes with air-hole diameter to pitch ratio, d/Λ, less than or equal 0.15. At short wavelengths, the fibers' performance is limited by macro-bending losses, which determines the practical wavelength range for applications. Another important PCF application is the efficient generation of broadband white light. The key advantage of such sources is that the light is spatially coherent, which means that it can be focused down to an almost diffraction-limited spot across its entire spectrum. This broadband supercontinuum (SC) generation is one of the most important development emerged from PCFs. The applications of this SC are found in wide area such as optical coherence tomography, frequency metrology, fluorescence lifetime imaging, optical communications, and many others. Other emerging PCFs applications are in sensing from chemical, biological, medical, to environmental, and high-power lasers and amplifiers.

Photonic crystal fibers optimized for single mode operation combined with a relatively large modal area are preferable to transmit high optical powers. Double-cladding concept has been used, where the pump cladding is surrounded by an air-cladding region. Due to the very large contrast of refractive index, the pump cladding can have a very high numerical aperture (NA), which can exploit inexpensive low-cost multimode diode as pumping device. Such PCF designs can also have very large mode areas of the fiber core while guiding only a single mode for diffraction-limited output, and are thus suitable for very high output powers with excellent beam quality. The core region can be doped by rare-earth dopant such as Erbium (Er), and Ytterbium (Yb), that works in near-infrared regions (at around 1060 nm for Yb-doped and 1550 nm for Er-doped). However, high power in fiber laser can induce thermal-effect which exhibits the internal temperature gradient in rare-earth-doped core that can influence the modal properties of the fiber which can affect especially the modal discrimination between the fundamental mode and higher order modes that is necessary for single mode operation. The proper PCFs fiber design is worth explored to overcome the thermal-effect to maintain the single mode operation of the fiber laser.

Up to date, the highest power fiber lasers have been achieved by Yb-doped silica fibers that operate at around 1 μm. But lasers in this wavelength range are invisible and can give a serious hazard if their power reach onto the retina. This can be a problem for some laser applications which facilitate the direct interaction with humans. Therefore, the thulium-doped silica fibers are preferable to be used due to their operation in the eye-safe wavelength region (> 1400 nm), where optical absorption by water in the eye prevents power from reaching the retina. To obtain high power laser, in principle, the same guidelines used for Yb-doped PCFs can be applied to Tm-doped PCFs. However, Tm-doped PCFs for fiber laser much suffers from quantum defect which is the energy difference between the pump and laser photons that causes a stronger refractive index gradient along the cross-section, which favors higher order modes (HOM) confinement, thus make it difficult to preserve the single mode operation. Therefore, a robust PCFs design is mandatory for high-power very large mode-area Tm-doped fibers. One interesting design solution, which has been recently applied to both air silica and all-solid LMA fibers with good results, is to break the

C_{6v} symmetry of the fiber cladding to improve delocalization of the most detrimental HOMs, while keeping the Fundamental Mode (FM) confined in the doped core.

1.2 PCFs in terahertz regions

The THz frequency range located midway between microwaves and infrared spectral regions in the region between 0.1 and 10 THz (3 mm to 30 μm), presents a virtually unexplored region of the electromagnetic spectrum. Therefore, this bandwidth is also known as the THz gap. THz research science and technology can be found either in the field of electronics or optics, or the combination of both. As the working wavelength is reasonably small, THz is preferable choice for imaging application due to the achievement of the resolutions up to sub milimeter. Moreover, THz photon energy is relatively small (E_p < 12.4 meV for f < 3 THz) which causes that THz radiation is safe without any concern of ionization of the sample. THz signatures of large macromolecular materials, such as drugs, explosives, and proteins [14][15], allowing them to take their unique fingerprint identification, including absorption frequencies, amplitude and phase [16]. As such, THz imaging has great potential in security screening, biosensing, quality control, forensic and medical applications.

The growth in scientific applications at THz frequencies has been driven by the development of Time domain THz spectroscopy (TDS) during late of 80's and Quantum cascades laser (75 THz in 1994 and 4.4 THz in 2002) [17][18]. These two inventions have played an important role in the eventual translation of THz applications from the research lab to the real world and have sparked a rapid growth in the field of THz. Despite the fast growth in THz technology, many supporting components are still in early stage of development. One of them is the availability of a broadband low-loss waveguide. Metal or solid core dielectric waveguides can not be used for this purpose due to the limited conductivity of metals and the prohibitively high absorption of dielectrics in the THz range.

Dielectric waveguides at optical frequencies take many forms and have been investigated at THz frequencies. Amongst the earliest examples were simple plastic ribbon waveguide [19], single crystal sapphire fibres [20] and sub-wavelength diam-

eter plastic fibres [21]. Guiding mechanisms in these structures take place by total internal reflection (TIR) at the core-air boundary with a significant fraction of the wave extending into the air. After the invention of photonic crystal fiber, the attention has been switched to apply this kind of fiber for THz waveguiding. PCFs were first developed in silica for near infrared applications and thanks to the excellent physical properties of silica, they can be produced with a precision at the wide variety of nanoscale forms. At THz frequencies, silica is very lossy. A variety of reasonably low loss polymers adaptable to fibre drawing can be substituted for short propagation lengths. THz polymer PCFs are fabricated using a similar processing with that used for silica PCFs. A macroscopic scale of the diameter (cm-diameter version), called a preform, is created by stacking tubes, either inside a jacket or the jacket is added later. The preform is then fused together and drawn down, extending its length and reducing its diameter to mm size with pressure applied to the core and capillaries to prevent tubes collapsing. The extrusion process have also been applied, enabling the formation of structures not readily attainable by stacking capillaries. The choice of polymer is very important because dielectric loss at THz frequencies is generally large. The lowest loss materials of choice are currently cyclic olefins, such as those with the trade names Zeonex and Topas, which have absorption coefficients of order 0.2 cm^{-1} at 1 THz. The transmission loss can be reduced further for long-length THz wave deliveries by considering the use of dry air in hollow-core PCFs designs with the goal to maximize the amount of field that propagates in air at the expense of that in the dielectric. PBG Hollow-core PCFs offer lower loss, but in limited bandwidth. However, in order to achieve the band gap effect for the guided core mode, the fundamental lattice that constitute the cladding needs to be repeated several times. This limits the minimum fiber size that can be achieved for the waveguide that affects its flexibility in THz setups. Since most of the applications proposed for the terahertz range require wide transmission bandwidths and flexibility, most of the waveguides that have been proposed in the literature rely on the IC confinement mechanism. In contrast with PBGs, an IC PCF doesn't exhibit any photonic bandgap and the confinement relies on a strong reduction of the coupling between core modes and cladding modes. This fibers allow ultra broadband guidance, although with relatively higher

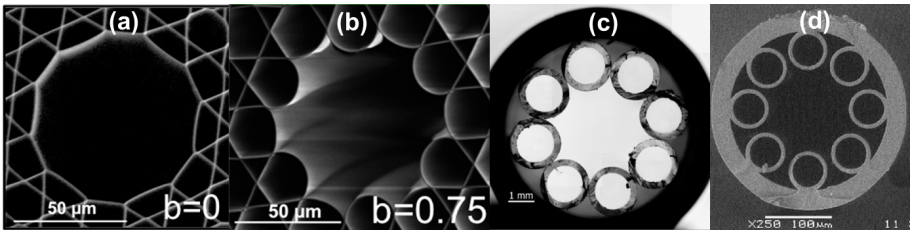

Figure 1.1: SEM images of inhibited coupling PCFs (a) Classical Kagome fiber [1] (b) Hypocycloidal kagome fiber [1] (c) Circular tube lattice fiber for THz [2] (d) Non-touching capillaries CTLF for mid-infrared region [3].

losses, typically 1 dB/m, than HC-PCFs with PBGs.

Fig.1.1 shows the inhibited coupling HC-PCFs. The third image (fig. (c)) is Inhibited coupling fiber for THz applications, while (d) is the example of inhibited coupling fiber for mid-infrared applications. The first inhibited coupling fiber introduced was the Kagome fiber which is the type of hollow core fiber with an inverted curvature of the optical core boundary. The guidance properties of Kagome Fibers depend on the thickness of the glass webs forming the cladding structure. The properties of Kagome fibers mainly depend on the first silica layer surrounding the optical core [22]. The hypocycloid-like contour in Kagome core-shaping has proved for fiber loss reduction. Fig.1.1(b) shows hypocycloidal kagome fiber with high curvature (expressed with high b-parameter [1]) than classic kagome fiber in (a) with 0 curvature. The hypocycloid-like contour with high curvature can be set to minimize the core and cladding mode coupling which further allows a significant reduction of the fundamental mode confinement loss. Fig.1.1(c) shows the first prototypes of circular tube lattice fibers (CTLFs) which consist of a hollow core surrounded by a circular arrangement of polymethylmethacrylate tubes [2].

Chapter 2

Large pitch fiber

2.1 Introduction

A great industrial demand for the high power laser has stimulated a great research effort for the improvement of the fiber laser technology in the last two decades. Fiber lasers are currently the most preferable solid-state laser concept due to their high efficiency, beam quality, and easy thermal management. Unfortunately, higher pulse energies in high-power fiber-lasers are accompanied by higher peak powers that cause nonlinear effects. To circumvent these nonlinear effects, fiber lasers require large effective mode area (LMA), while maintaining single mode operation. One approach that provides large mode areas and single-mode operation is fiber designs that allow high losses for the higher order modes. This capability of delocalizing the HOMs from the core causes the fiber to propagate only the fundamental mode after some length, thus the fiber laser provides single-mode operation. Large Pitch Photonic Crystal Fiber, short called by Large Pitch Fiber (LPF) [11], has their pitch Λ, i.e. hole-to-hole distance, is larger than 10 times the operating wavelength λ. The fibers have hexagonal PCF structure, with the core can be surrounded by one, two or three rings of air holes [23]. These fibers have large mode area (LMA) and achieve the delocalization property, and consequently HOMs suppression, granted high output power and good beam quality.

LPFs use large holes approach and this kind of fiber design introduces the 'modal sieve' concept with propagation loss for each mode [24]. Some different design parameters that define the structure of LPFs are: the hole-to-hole distance or pitch Λ, the relative hole size d/Λ, the number of missing holes creating the core, and the number of rings of holes forming the cladding. In this fiber design, the modal discrimination mechanism is defined by differential propagation losses. As the spatial size of the transverse modes decreases with higher modal order, these higher-order modes can escape from the guiding structure more easily and exhibit an increased propagation loss than the fundamental mode. Effective single-mode operation can be thus obtained by modifying fiber parameters to the fiber length and to the required higher-order mode suppression. In the case of double-cladding LPFs, the modal discrimination can be determined by the difference of the overlap integral between the fundamental mode and the higher order modes. In this kind of fibers, the two rings design provides based compromise between modal discrimination, i.e. the HOM suppression, and beam quality [23].

The objective of this chapter is to provide a numerical analysis based on finite element method to investigate the delocalization properties of LPF family. This chapter will cover simple analysis of modal properties and overlap integrals of the fiber design structures to investigate their delocalization properties. This chapter will not cover the influence of index depression in the core region due to the rare-earth doping in the active core region and the thermal effect due to high energy power in fiber laser that will effect the modal properties and modal discrimination, thus the delocalization properties of the fiber. These discussions will be the subjects of the next chapter. Results show that the LPFs possessing the core formed by one missing-holes provide delocalization properties of higher order modes. Scaling these kinds of fibers to obtain larger mode area, the fibers maintain the delocalization properties. On the contrary, obtaining larger mode area, by additional missing-holes forming the core of the LPFs, e.g. with 7-missing holes, the fibers exhibit poor delocalization properties, due to the higher order modes become more confined in the core.

2.2 Finite Element Method

The complex geometry of PCF structures, make them difficult to analyse mathematically. Standard optical fiber analyses do not help. In practice, it is preferable to solve Maxwell's equations numerically, rather than analytically. In particular, to achieve the solutions of the Maxwell equations in the PCFs, the Finite Element Method (FEM) is useful. The basic idea of FEM is to split the 2D domain of electromagnetic problem, in this case it is represented by the optical cross-section, in a large number of triangular elements called by mesh. Over the mesh the differential electromagnetic problem can be discretized, locally linearized and finally solved. The well-known curl-curl equation:

$$\overline{\nabla} \times (\overline{p}\overline{\nabla} \times \overline{H}) - k_0^2 \overline{q}\overline{H} = 0 \tag{2.1}$$

being H the magnetic field, k_0 the wavenumber of the vacuum, p the inverse of relative permittivity tensor, q the relative permeability tensor, can be transformed, using the variational Rayleigh-Ritz approach (after Walther Ritz and Lord Rayleigh) and the Webb edge elements formulation [25], into a generalized eigenvalues problem:

$$([T] + n_{eff}^2[S])\{h\} = 0 \tag{2.2}$$

being $[S]$ and $[T]$ large, sparse, symmetric and not positive matrices, and the eigenvalues are the square of the effective index. In this chapter an in-house developed full-vector modal solver, based on FEM, has been used to analyze the LPFs. The solver software can obtain both real and complex solutions of electromagnetic problem, implementing the Perfectly Matched Layers [26] in the domain boundary. The solver can also calculate the effect of bending in the structure and solve overlap integrals. The validity of the simulation results obtained by the software have been tested in comparison with a commercial one [27]. The performed tests show that the developed solver achieves correct solutions for the electromagnetic problem in optical devices with the different results in the level of 10^{-7}. The software also achieves excellent performance in term of required memory space and execution time.

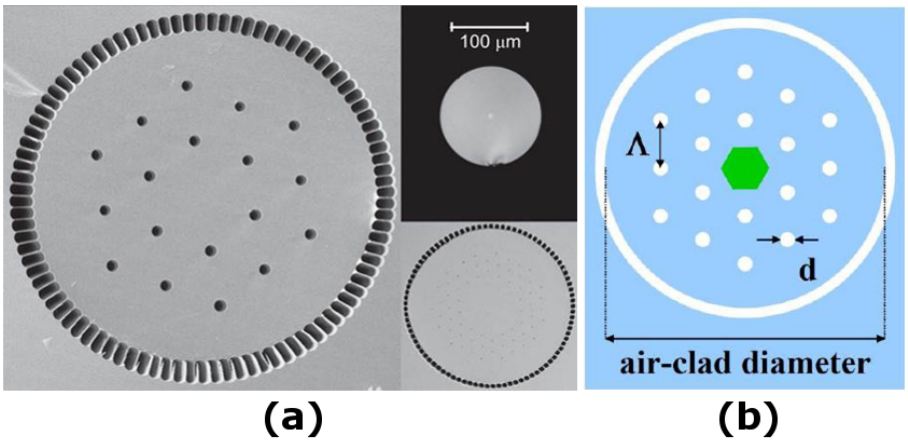

Figure 2.1: LPF (a) SEM pictures [4] (b) LPF parameters

2.3 Structures

Fig. 2.1(a) shows the comparison of a 135-μm core LPF (left) with a 7-μm core step index fibre (upper right) and a conventional rod-type PCF (lower right), in the same scale of SEM pictures. This picture illustrates the enormous core area scaling of LPF with the simplicity of the structure. The core area of the LPF is comparable with the 125-μm outer cladding of the step-index fibre. The rod-type PCF was the representative of VLMA fibres, which achieved an active core diameter as large as 80 μm from which single-mode emission could be extracted. With its arrangement of tiny air holes which is a necessary condition for the effective single-mode operation of these kinds of fiber, the reproducible fabrication is extremely challenging. This reproducibility issue results in a low yield, which increases the costs.

For a step-index fibre and a rod-type PCF, all of the transverse modes have significant overlap with the core area, which means all of the modes are confined in the core. As seen in the picture, the inner structure of a LPF is rather open as a results of large air holes and pitch. Strong deformations of the higher order modes results in weak overlap with the core region. Thus only the fundamental mode with the Gaussian-like profile has a substantial overlap with the core.

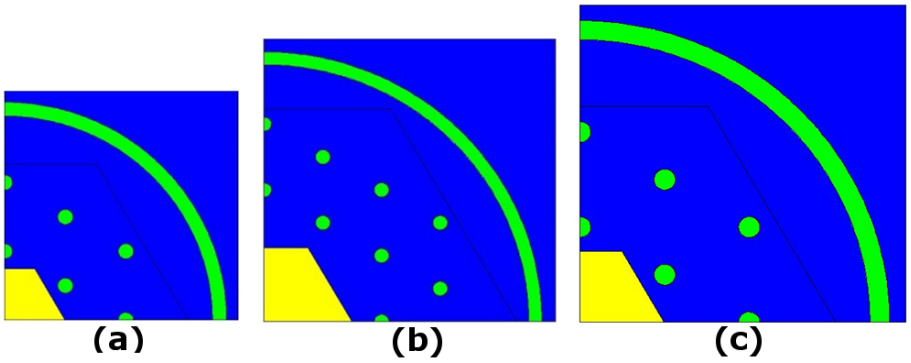

Figure 2.2: LPF (a) LPF-30 (b) LPF-30 modified (c) LPF-45

The fiber structures under investigation are described in Fig. 2.2 and Fig. 2.3 with the fiber parameters described in Fig. 2.1-(b). Only one quarter of the fiber structures are needed to be simulated due to symmetry properties of LPFs. LPF-30 has the pitch $\Lambda = 30\ \mu$m, and the ratio between air hole and pitch $d/\Lambda = 0.22$, where d is the hole diameter. The core area is formed by 1-missing hole, and the fiber has air-cladding with the radius of 89.07 μm. The fiber is then modified by enlarging the core (see Fig. 2.2-(b)), and in this way enlarging the modal area, with 7 missing air-holes, and consecutively added with external air holes rings to maintain the two rings of air-holes in the cladding. The fiber has been called by LPF-30 modified with the air-cladding

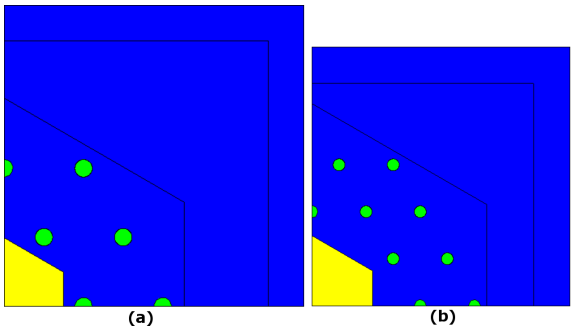

Figure 2.3: LPF without air-cladding (a) LPF-45 (b) LPF-30 modified.

Description	LPF-30	LPF-30 Modified	LPF-45
The normalized hole-diameter, d/Λ	0.22	0.22	0.22
The pitch, Λ	30 μm	30 μm	45 μm
Formation of the core	1 missing-holes	7 missing-holes	1 missing-holes
Number of air-holes ring	two	two (taken from 3^{rd} and 4^{th} original rings)	two
The core hexagonal edge	25.84 μm	38.76 μm	38.6 μm
The large hexagonal edge	78.52 μm	111.89 μm	117.78 μm
Air-clad inner radius and width	89.07 μm, 5.88 μm	117.06 μm, 5.88 μm	133.6 μm, 9.1 μm
Materials	Silica, $n_{eff} = 1.45$	Silica, $n_{eff} = 1.45$	Silica, $n_{eff} = 1.45$

Table 2.1: LPF Characteristics

radius 117.06 μm. Fig. 2.2-(c) shows LPF-45 which is the scaling version of LPF-30 by maintaining d/Λ to obtain a structure with a pitch of 45 μm, air cladding radius 117.78 μm. Table 2.1 describes the detail parameters of the fiber structures. The fiber structures without air-cladding and with the same parameters are evaluated for LPF-30 modified and LPF-45 to investigate the propagation loss comparison between the two structures. These fibers are described in Fig. 2.3 with Perfectly Matched Layers (PML) have been applied as the absorbing boundary.

2.4 Results and Analysis

Graph in Fig. 2.4 shows the effective index versus wavelength for a range of 960-1100 nm of the Double-cladding LPFs described in Fig. 2.2. Despite of the fiber structures, the effective indices have a linear relation with the wavelength both for the fundamental modes and the first higher order modes. The overlap integral has been used to investigate the modal discrimination between the fundamental mode and the first higher order mode of the two approaches of enlarging the large mode: removing the 7 missing-holes in core or scaling the fiber structures while maintaining the normalized hole-diameter, d/Λ = 0.22. The overlap integral Γ over the core area has been calculated according to the expression

$$\Gamma = \iint_S i(x,y)\,dxdy, \tag{2.3}$$

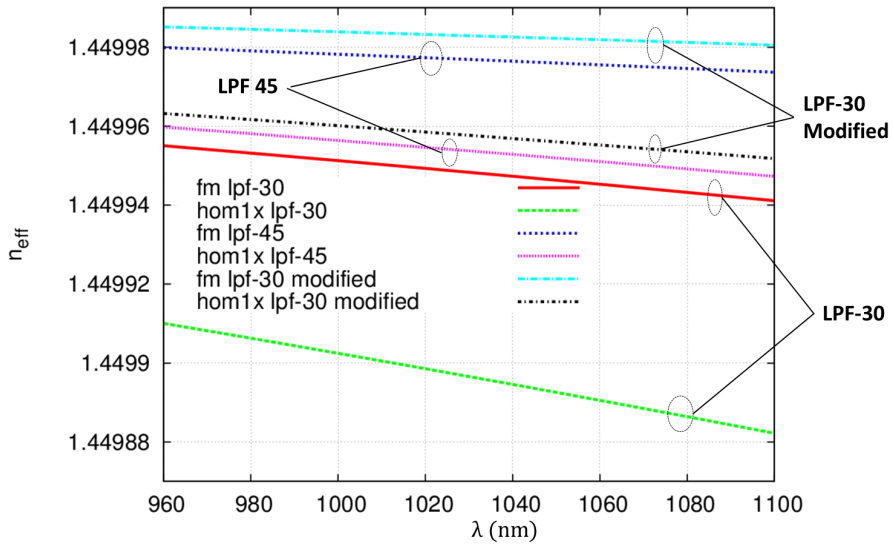

Figure 2.4: Effective index of LPF

being $i(x,y)$ the mode normalized intensity distribution and S the core region [28]. The modal discrimination $\Delta\Gamma$ between the FM and the most confined HOM, which is the difference of the overlap integral values, has been used to asses the single mode (SM) properties. A value of $\Delta\Gamma$ higher than 0.3 has been assumed to be sufficient to provide enough suppression of the HOMs in the gain competition to ensure SM guiding [29][30]. From the results, LPF-30 modified exhibits higher overlap integral for the first HOM than LPF-45, while the overlap integrals of the fundamental modes for both fibers are similar. As an example at λ = 960 nm, the first HOM of LPF-30 modified has 0.64 overlap integral while the LPF-45 one has 0.22. In this wavelength, the fundamental modes for both fibers have 0.84 of overlap integral. The modal discrimination between the FM and the first HOM of LPF-30 modified ($\Delta\Gamma$) is around 0.20, thus lower than the sufficient value to provide the HOM suppression. On the contrary, LPF-45 experiences the modal discrimination of around 0.60 which is much higher that the sufficient value. Clearly, the LPF-45 structure promises as a suitable PCFs design for large modal area fibers, while maintaining the single mode

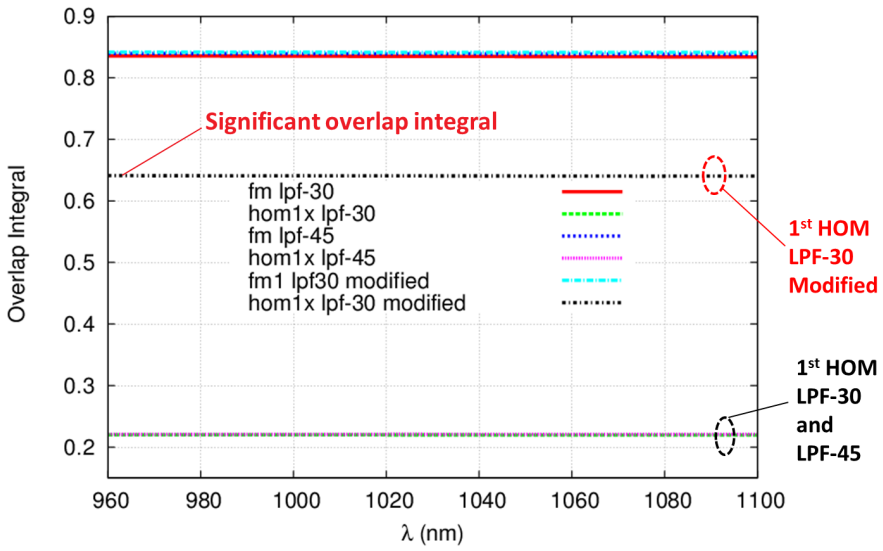

Figure 2.5: Overlap integral of LPF

operation. These kinds of fibers are suitable for high power fiber laser applications.

Air-cladding in PCFs have been used to confine pump light to the multimode pump core, which is the fiber area inside the air-cladding. The large index contrast between the air-cladding and the material inside enables higher numerical apertures for the coupling of pump light into the pump core, determined by the bridge-width in the air-cladding. In term of cost point of view, the fibre laser can exploit the relatively low-cost multimode diode as pumping device. Here, the multimode pump core is suspended by very thin struts in the air-cladding, through which the pump light cannot escape. In the simulation, the air-cladding is approached by neglecting the strut by applying the air as the overall material. Fig. 2.6 shows the magnetic field modulus of LPF-30 modified and LPF-45. Despite of the structures, the fundamental modes are confined in the core. On the contrary, the first HOM of LPF-45 is evident less confined than the LPF-30 modified one. The fundamental modes of both fibers have the overlap integral around 0.84, while the overlap integral of the first HOM of LPF-45 is 0.22 less than the one of LPF-30 modified, which is 0.64 (see Fig. 2.5). The

leakage of the field of LPF-45 is also evident from the two peaks of magnetic field modulus outside the cladding area, near the air-cladding. The fields cannot escape from air-cladding due to the high index contrast between cladding and air-cladding.

In order to investigate the fiber loss, the air-cladding have been removed and the Perfectly Matched Layers have been applied to LPF-30 modified and LPF-45. Fig. 2.7 shows effective index n_{eff} of LPF-45 and LPF-30 modified. LPF-30 modified has higher effective index for FM and HOM than LPF-45, with the difference of effective index of FM is more evident than the first HOM one. Removing the air-cladding has been highlighted that the modes in LPF-45 have important losses as described in Fig. 2.8, including the fundamental mode. The FM of LPF-45 has a significant loss around 2.5 dB/m. The figure also confirm that the first HOM of LPF-45 with PML has high significant loss than LPF-30 modified, for example the loss achieves 95.96 dB/m for LPF-45 at λ = 960 nm, while for LPF-30 modified, the loss for the first HOM at the same wavelength is only 1.13 dB/m. The LPF-30 has very lower loss for fundamental mode, for example at λ = 960 nm the FM has α = 0.085 dB/m. Fig. 2.9 shows the magnetic field modulus of the FM and the first HOM of both both fibers. Here, it is clear that the first higher order mode of LPF-30 modified is more confined in the core region, thus the fiber exhibits lower modal discrimination between the FM and the first HOM.

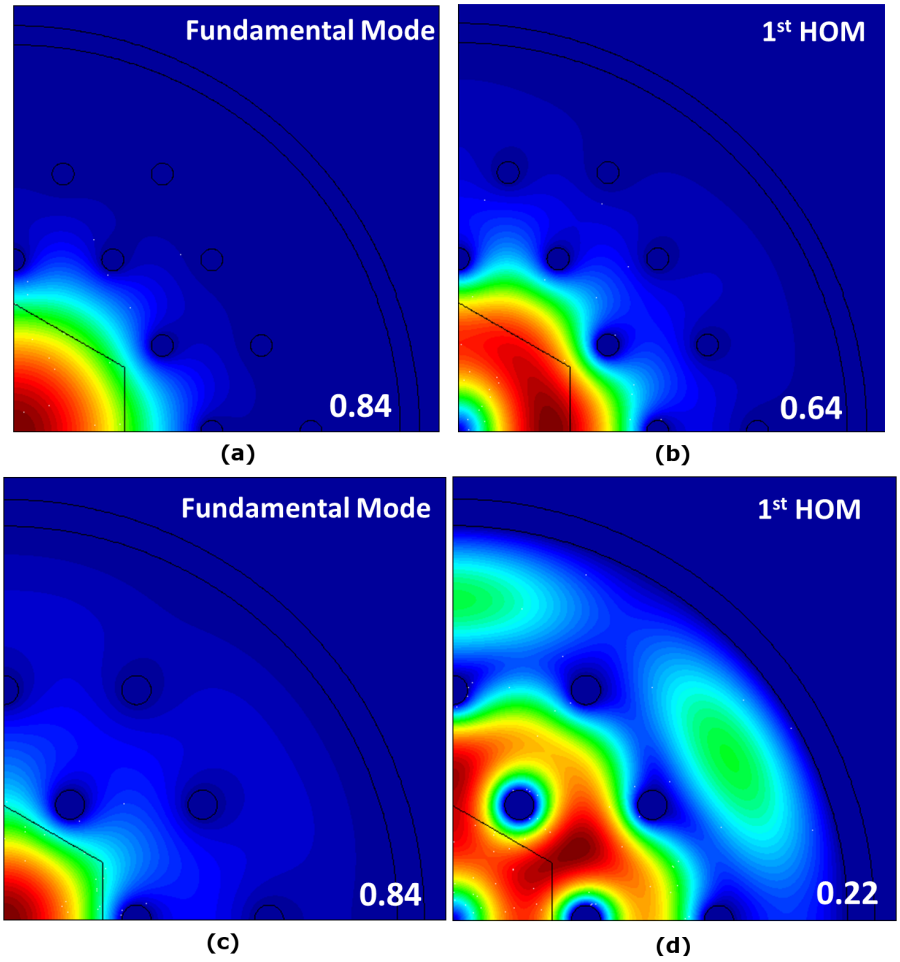

Figure 2.6: Magnetic field modulus of LPF-30 modified (top): (a) FM (b) First HOM ; LPF-45 (bottom): (c) FM (d) First HOM.

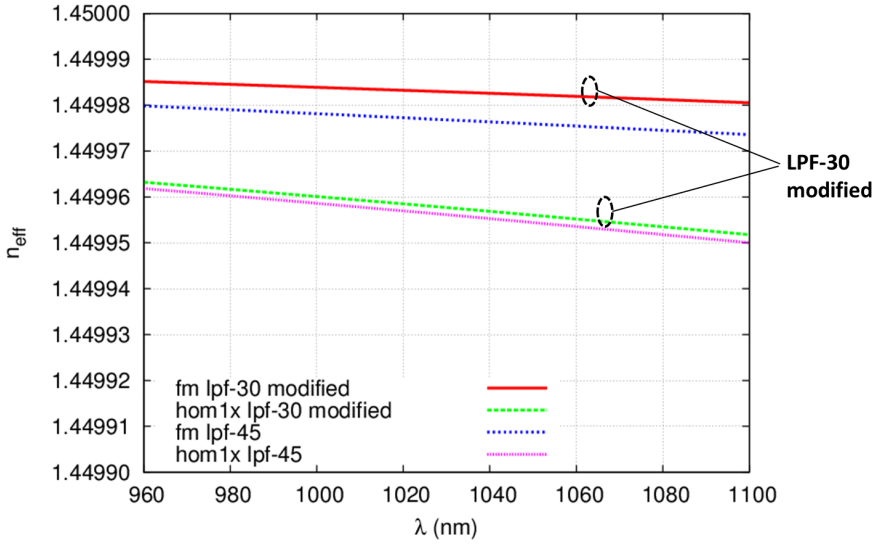

Figure 2.7: n_{eff} of LPF with PML

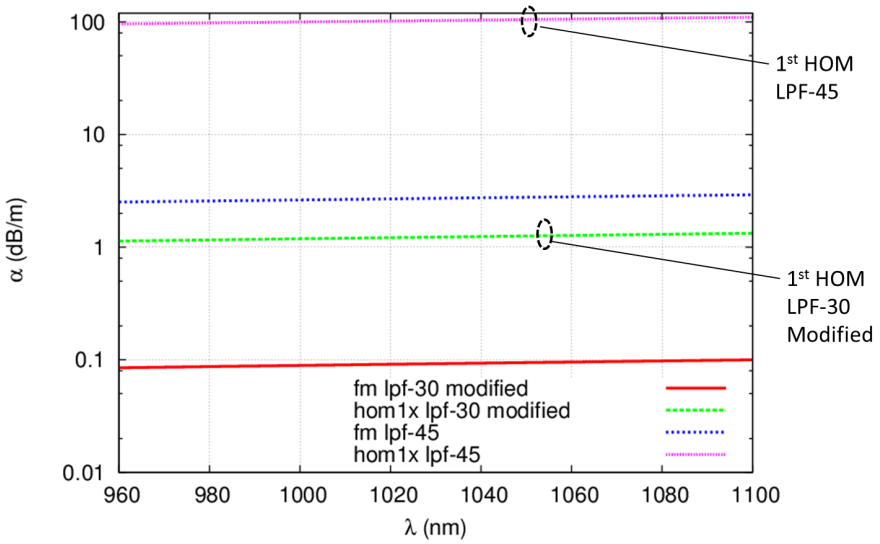

Figure 2.8: Propagation loss α of LPF with PML

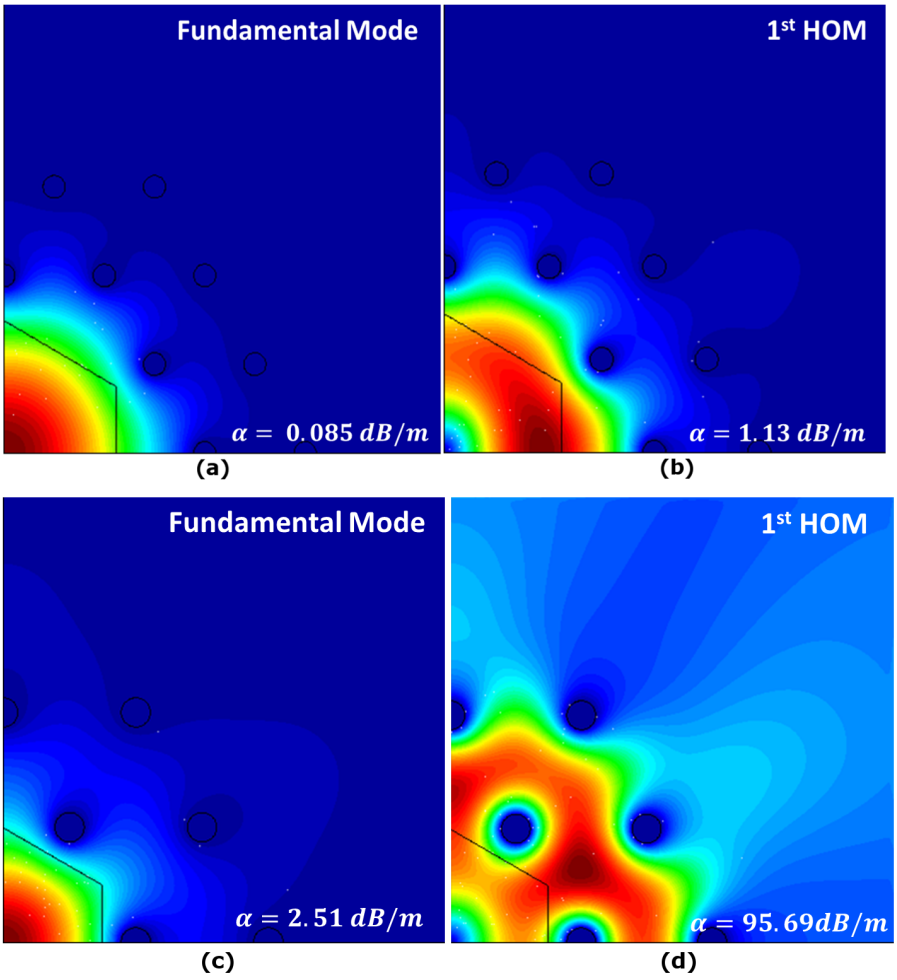

Figure 2.9: Magnetic modulus of LPF with PML, LPF-30 modified (top): (a) FM (b) First HOM ; LPF-45 (bottom): (c) FM (d) First HOM.

Chapter 3

Symmetry-free PCF

3.1 Introduction

Several applications requiring long range propagation such as remote sensing, communication, industrial processing and defense, are currently pushing the research of high power sources in the 2 μm - 3 μm range, which also attractive thank to the eye-safe nature of the scattered light at these wavelength [31]. Thulium-doped fiber lasers are of particular interest for these applications, being able to combine high brightness, premium beam quality and compactness, together with the possibility to obtain emission on a relatively wide band, spanning from at least 1.86 μm to around 2.09 μm, when pumped with established diode lasers emitting at 0.79 μm. Thulium-doped fiber lasers are also interesting for medical applications due to the strong absorption of water at 1.94 μm.

The constraint to produce the highest possible power of fiber laser with diffraction-limited output has stimulated a huge research effort for the improvement of high power fiber lasers in the last decade. The fiber laser have changed the attraction of research communities and industries beyond the telecommunication application stimulated by the invention of double cladding concept for multimode pumping that enable to boost the fiber laser power into watt level. But then fiber core diameter in truly single mode fibers limits fiber output power beyond 100 W [32]. Large

mode area (LMA) fiber designs investigated around the year 2000 enable immense growth of output power up to 1 kW output in $\sim$1 μm exploiting the excellent spectroscopic properties of Yb [33]. Greater core area known as very large mode area fibers (VLMA), being mode field diameter greater than 50 μm, have further been proposed implementing leakage channel fiber concept [34] and large pitch PCF (LPF) [23] to increase the fiber laser power while maintaining the single mode operation by delocalizing the higher order modes. Using LPF with mode field diameter $\sim$105 μm fiber based ultrashort pulse laser have achieved 3.8 GW peak power [35] when combined with chirped-pulse-amplification technology.

Up to date, the highest power fiber lasers have been achieved by Yb-doped silica fibers that operate at around $1\,\mu m$. But lasers in this wavelength range are invisible and can give a serious hazard if their power reach onto the retina. This can be a problem for some laser applications such as soft-tissue medicine which facilitates the direct interaction with humans. Therefore, the thulium-doped silica fibers are preferable to be used due to their operation in the eyesafe wavelength region ($> 1400\,nm$), where optical absorption by water in the eye prevents power from reaching the retina. To obtain high power laser, in principle, the same guidelines used for Yb-doped PCFs can be applied to the design of Tm-doped fibers [36][37], with the advantage that operation at longer wavelengths allows SM propagation with larger effective area, therefore pushing the threshold for nonlinear phenomena towards higher power levels. Nevertheless, the development of PCFs with robust single-mode operation and very large mode-field diameter, preferably exceeding $50\,\mu m$, for high peak power pulsed sources is hindered by the much larger quantum defect of Tm ions with respect to Yb, that causes remarkable heating of the doped core at relatively low pump power. The consequent thermal gradient along the fiber cross-section is responsible for an increase of the refractive index with a parabolic shape in the core and a logarithmic decay in the cladding, which severely alters the modal properties [38], allowing propagation of High-Order Modes (HOMs). A mitigation of the quantum defect and an increase of the laser efficiency can be obtained by exploiting cross-relaxation [39], but the high Tm concentration required for these process to occur results in an increased index contrast between the core and the cladding, which is detrimental to

SM properties [31].

As a consequence of the strong thermal effects, the adaptation of active PCFs conceived for operation at $\sim$1 μm to Tm-doped devices is not straightforward, and new design approaches are worth exploring. One interesting solution, which has been recently applied to both air silica and all-solid LMA fibers with good results, is to break the C_{6v} symmetry of the fiber cladding to improve delocalization of the most detrimental HOMs, while keeping the Fundamental Mode (FM) confined in the doped core [40][41]. In this paper the design of a Tm-doped DC-PCF with Symmetry-Free cladding (SF-PCF) and a core diameter of $\sim$80 μm is presented, and the fiber guiding properties are thoroughly analyzed by means of a full-vector modal solver based on the finite-element method [42]. Moreover, a thermal model is applied to investigate how thermally-induced refractive index change affects the SM properties [43]. The results are compared with those obtained for a Large-Pitch Fiber (LPF) with similar core size, which represents the current state-of-art of large-mode area Tm-doped fibers [44].

3.2 Thermal effects modelling

The guided modes for the fiber design have been calculated using a FEM based full-vector modal solver. The refractive index of the triangle element has been set according to the thermo-optic properties of silica. Silica has linear temperature dependence of the thermo-optics effect. Heat equation is obtained by approximating the actual PCF cross-section with simple four concentric layers corresponding to core, inner cladding, air-cladding and outer cladding. Fig. 3.1 shows the model and the graph of Δn. Each layer has isotropic thermal conductivity k_i and radius r_i. Heat power density Q_0 [W/m^3] is generated from the core, which is related to the heat load per unit length q' according to

$$q' = Q_0.A_{core}, \tag{3.1}$$

being A_{core} the doped core area.

The steady state heat equation can be solved by considering only the transverse coordinates, and further simplified into a function of the distance r from the core

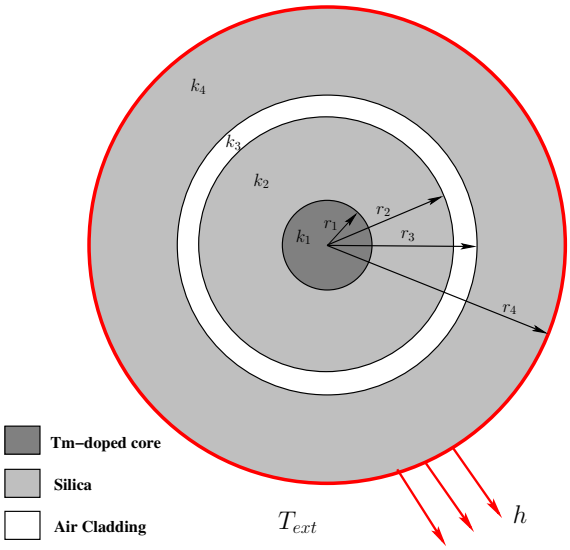

Figure 3.1: Thermal-effect modelling

center due to the radial symmetry of the model:

$$\frac{\partial}{\partial r}\left(r\frac{\partial T(r)}{\partial r}\right) = -\frac{Q}{k_i}, \tag{3.2}$$

where the generated heat density Q is Q_0 in the core and 0 elsewhere, being $T(r)$ the local temperature. Thermal conductivity $k_{SiO_2} = 1.38$ W/(m.K), which is the one of fused silica, has applied in the core, inner cladding, and outer cladding regions. The contribution of air-holes to the overall heat transfer is assumed to be negligible due to their relative small sizes. On the contrary, the air-cladding requires the definition of thermal conductivity k_{AC} because of its relative large size with respect to the silica struts according to:

$$k_{AC} = k_{air} + \frac{N.w.k_{SiO_2}}{2\pi(r_3 - r_2)} ln\left(\frac{r_3}{r_2}\right) \tag{3.3}$$

being $k_{air} = 0.02$ W/(m.K) the thermal conductivity of air, N and w are the number and width of air-cladding struts, r_2 and r_3 the inner and outer air-cladding radii, respectively. The value of k_{AC} has been found to be 0.087 W/(m.K) for the fiber design.

Heat dissipation has been assumed to apply at the outer fiber boundary, with coefficient $h = 2000$ W/(m^2.K) corresponds to water-based quenching cooling system. Using Newton's law of cooling:

$$\frac{\partial T(r=R)}{\partial r} = \frac{h}{k_{SiO_2}} [T_{ext} - T(R)] \tag{3.4}$$

where R outer fiber radius and the fiber external temperature is $T_{ext} = 14^oC$. The refractive index change Δn_{th} of silica and doped silica due to thermo-optical effect is finally obtained as $\Delta n_{th} = \beta [T(r) - T_a]$, being $\beta = 1.16 \times 10^{-5}$ 1/K the thermo coefficient of silica and $T_a = 25^oC$, ambient temperature.

3.3 SF-PCF Analysis

The schematic of the considered SF-PCF cross-section is reported in Fig. 3.2(a). The inner cladding is obtained from a common triangular lattice where several air-holes have been removed to form two hexagonal layers, rotated with respect to each other. Three more air-holes, marked with arrows in the picture, have been kept to further weaken symmetry of the cross-section, similarly to what was done with the all-solid fiber in [29]. The 19 innermost unit cells are replaced with Tm-doped silica elements to obtain the active core. The DC SF-PCF considered in the simulations is shown in Fig. 3.2(b), where the key parameters are also indicated. All the considered symmetry-free fibers have a underlying lattice pitch Λ_{SFF} = 14.4 μm, which is also the distance between closest air-holes. The fiber core has a corner-to-corner distance d_{cc} of about 80 μm, which would be the distance between corner air-holes if the structure were not rotated with respect to the triangular lattice, and the edge a of resulting doped hexagonal region is 36 μm. A 6 μm-thick air-cladding with inner radius of 260 μm surrounds the cross-section, to provide pump guiding. To assess the advantages provided by the SF-PCF over current state-of art fibers, the simulation results have been compared with those obtained with the LPF shown in Fig. 3.2(c), which is characterized by hole-to-hole spacing Λ_{LPF} = 45 μm, core corner-to-corner distance $d_{cc} \approx 81$ μm and doped region with edge a = 31.5 μm [44]. Down-doping of

the active region to compensate for the thermally-induced refractive index increase has been taken into account for both fibers.

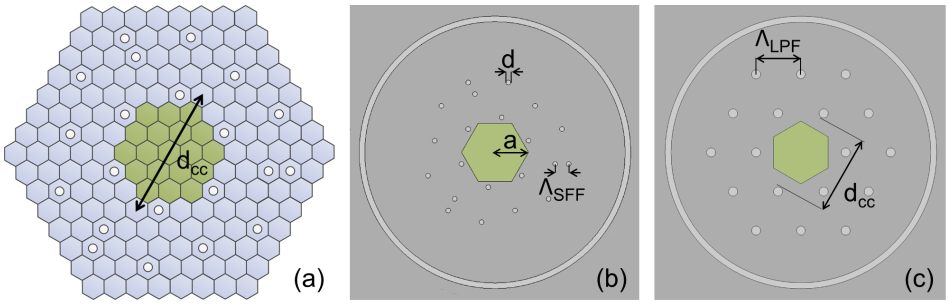

Figure 3.2: (a) Schematic of the cross-section of the symmetry-free PCF. Cross-sections of the simulated (b) symmetry-free and (c) large-pitch fibers.

The degree of confinement of the guided modes has been evaluated considering their overlap integral Γ over the doped area. The modal discrimination $\Delta\Gamma$ between the FM and the most confined HOM, which is the difference of the overlap integral values, has been used to asses the SM properties. The same assumptions of a $\Delta\Gamma$ value higher than 0.3 has been taken to provide enough suppression of the HOMs in the gain competition to ensure SM guiding.

Both the SF-PCF and the LPF have been assumed to be 1 m-long rod-type fibers, with outer diameter of 1.7 mm. Convection cooling with forced water flow at the temperature of $14^o C$ and convective transfer coefficient $h = 2000$ W/$(m^2.K)$ has been applied as boundary condition at the outer fiber edge. Temperature gradient on the fiber cross-section is generated by quantum defect-heating of the active core, which is responsible of a heat load q'.

$$q' = \frac{1 - 10^{-\alpha \frac{dL}{10}}}{dL} \cdot \left(1 - \frac{\lambda_p}{\lambda_s}\right) \cdot P, \tag{3.5}$$

being α = 9 dB/m the pump absorption, λ_p = 793 nm the pump wavelength, λ_s the emission wavelength, dL the fiber length where the average optical to heat energy conversion is calculated and P the pump power [45]. Heat load is related to heat density Q_0 by the relation in Eq. 3.1. q' values between 0 W/m and 340 W/m have been

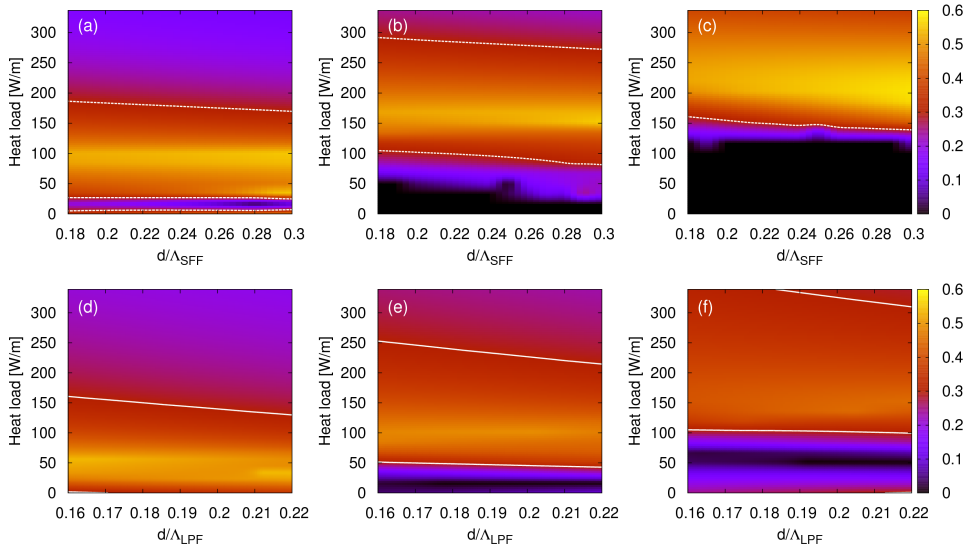

Figure 3.3: Overlap integral difference $\Delta\Gamma$ between the FM and the most detrimental HOM of the SF-PCF, as a function of the normalized air-hole diameter and heat load, obtained with (a) no core down-doping, (b) with core down-doping $\Delta n = -10^{-4}$, and (c) with $\Delta n = -2 \cdot 10^{-4}$. Same results obtained for large-pitch fibers are reported in (d) for no core down-doping, (e) for $\Delta n = -10^{-4}$ and (f) for $\Delta n = -2 \cdot 10^{-4}$. White lines are drawn at $\Delta\Gamma = 0.3$.

considered for the simulations, which correspond to the average heat load obtained from Eq. 3.5 in the last 10 cm of the fiber closer to the pumping end, for a coupled pump power P between 0 and 300 W.

3.4 Single mode regime

In order to optimize the SF-PCF design to provide the best SM properties in different operating scenarios, the $\Delta\Gamma$ value has been calculated for different choice of the air-hole diameter d between $0.18\Lambda_{SFF}$ and $0.30\Lambda_{SFF}$, taking into account heat load values spanning from 0 W/m to 340 W/m. $\lambda = 2$ μm has been considered as operat-

ing wavelength and 80 modes have been calculated for each parameter combination to find the most confined ones. The simulation results are shown in Fig.3.3(a)-(c), for a core down-doping $\Delta n = 0$, -10^{-4} and $-2 \cdot 10^{-4}$, respectively. The same procedure has been applied to the large-pitch fiber for d/Λ_{LPF} values between 0.16 and 0.22, and the results are shown in Fig. 3.3(d)-(f).

Clearly, none of the considered designs of the SF-PCF or LPF is able to provide SM guidance over the full range of considered heat load values. All fibers show a similar temperature dependent behavior, which is more evident in down-doped fibers. At low heat load values, for example approximately below 80-100 W/m for the SF-PCFs with $\Delta n = -10^{-4}$ of Fig. 3.3(b), the confinement of the FM is poor and its overlap integral is close the one of the HOMs, which is below 0.4 in most cases. In some extreme conditions, corresponding to the black areas of Fig.3.3(b) and 3.3(c), the overlap integral of the most confined HOM is even higher than the one of the FM. All the modes propagate mostly outside from the doped core, and poor amplification efficiency is expected. As the heat load increases the FM becomes significantly better confined than the HOMs, and the modal discrimination increases up to the maximum value, which is found at about 150 W/m for the SF-PCFs with Δn = -10^{-4}. After that point, any further increase of the core temperature decreases the modal discrimination by providing better confinement to the HOMs, up to the point where $\Delta\Gamma$ is again below 0.3 and the fiber operates in multimode regime.

By comparing Fig.3.3(a)-(c) it is possible to notice that SM operation can be shifted to significantly higher power levels by acting on core refractive index. Indeed, the SF-PCF without core down-doping can provide SM propagation for heat load between about 25 W/m and 180 W/m, while with $\Delta n = -10^{-4}$ the SM regime is found between $\sim$90 W/m and $\sim$290W/m and from $\sim$150 W/m up to more than 350 W/m for $\Delta n = -2.10^{-4}$. This means that a SF-PCF with suitable core down-doping is capable to maintain SM propagation even with a coupled pump power larger than 300 W. On the other side, the use of a too depressed core is detrimental for the operation at low pump power, and therefore core refractive index must be chosen according to the application. It is worth noting that in a real-world scenario the heat load is not uniform along the fiber, being significantly lower far away from the pumping

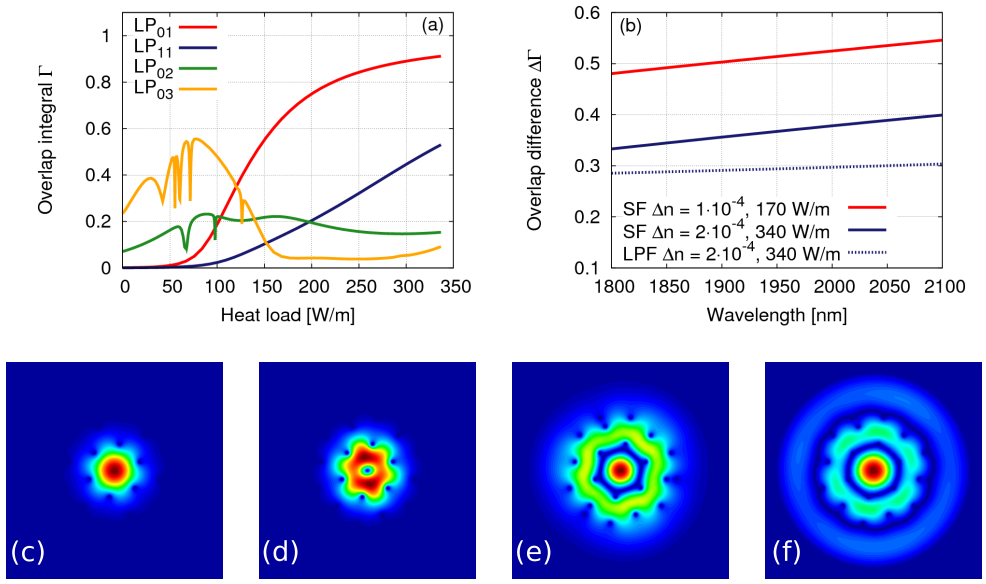

Figure 3.4: (a) Overlap integral of the most relevant guided modes of the SF-PCF as a function of the heat load, calculated at $\lambda = 2$ μm. (b) $\Delta\Gamma$ between the LP_{01}-like and the LP_{11}-like modes of the SF-PCF (solid lines) and of the LPF (dashed lines). Magnetic field modulus distribution of the (c) LP_{01}-like, (d) LP_{11}-like, (e) LP_{02}-like and (f) LP_{03}-like modes of the SF-PCF.

end, that is at the seed side assuming a counter-propagating pumping scheme. As a consequence, the FM is less confined and its overlap with the doped area is lower, resulting in a decrease of the amplifier efficiency. Considering the results of Fig.3.3, it is thereby preferable to choose a fiber design that allows operation close to the upper edge of the SM region at the pumping end, so that FM confinement and SM regime are preserved throughout most of the fiber length.

Air-hole size has a weaker impact on the guiding properties of the SF-PCF with respect to down-doping, resulting in a small shift of the SM region towards lower heat load values for increasing $d/_{SFF}$, that can be explained with the increased index contrast of the fibers with largest air-holes.

The main advantage of the SF-PCF approach is the possibility to provide very high modal discrimination at high pump power levels. The maximum value of $\Delta\Gamma$ achieved is above 0.54 for all the three considered values of core down-doping, and it is found at a heat load of about 100 W/m, 150 W/m and 200 W/m for the fibers having Δn = 0, -10^{-4} and -2.10^{-4}, respectively. Remarkably, similar mode discrimination has been reported for the all-solid version of the symmetry-free fiber without considering thermal effects [9], and is among the highest values reported so far for any index-guiding LMA fiber design. By choosing a suitable level of core down-doping it is possible to obtain SM guiding at high heat load also with the LPF, but the index depression is detrimental to the modal discrimination, as can be inferred by the comparison of Fig.3.4(d) and Fig.3.4(f). Indeed, with the LPF without core down-doping it is possible to reach a $\Delta\Gamma$ value larger than 0.5 at about 50 W/m, while a maximum overlap difference of only 0.42 is obtained with a core down-doping of -2.10^{-4}.

To give a deeper insight on the effect of fiber heating on mode confinement, Fig.3.4(a) reports the overlap integral of the four most relevant modes of the SF-PCF, calculated at λ = 2 μm for the fiber with $d/_{SFF}$ = 0.24 and Δn = -2.10^{-4}, as a function of the heat load. Notice that when the fiber is relatively cold both the fundamental LP_{01}-like mode, whose field intensity distribution is shown in Fig.3.4(c), and the LP_{11}-like one, shown in Fig. 3(d), are poorly confined, with Γ values below 0.2. Under this heating conditions the mode with the highest overlap is the LP_{03}-like, shown in Fig.3.4(f), whose overlap integral may even exceed 0.5. This behavior is due to core down-doping, which causes the modes that are naturally localized in the core to be poorly guided due to the lower refractive index of the doped region with respect to the cladding. The increase of the heat load compensates the core down-doping, improving the confinement of the LP_{01}-like mode while decreasing the overlap integral of the LP_{03}-like one. The FM has the highest overlap integral for q' higher than 120 W/m and its value rapidly increases with the heat load. Between $q' = 145$ W/m and $q^{'} = 200$ W/m the role of the most detrimental HOM is played by the LP_{02}-like, shown in Fig. 3(e), whose Γ value is anyway below 0.25. As a consequence, for $q' >$ 150 W/m the SF-PCF is SM. Finally, at very high power levels the thermally-induced

refractive index gradient is so strong to force the fiber to behave effectively as graded-index C_{6v}-symmetric waveguide. For $q' > 200$ W/m the LP_{11}-like HOM becomes the most detrimental one, its overlap integral increasing almost linearly with the heat load beyond this heat load value. Finally, it is worth noting that this SF-PCF is not only capable of providing strong delocalization of the HOMs even at high thermal load, but also to guarantee tight FM confinement, with overlap higher than 0.9 at $q' > 225$ W/m.

In order to demonstrate that the good HOM suppression properties of the SF-PCF are maintained over the whole spectrum of interest for Tm emission, the modal discrimination between the FM and the LP_{11}-like HOM has been calculated between 1800 nm and 2100 nm in two representative cases, and compared with the results provided by a LPF. Simulations have been performed on a SF-PCF with $d/SFF = 0.24$ and core down-doping Δn = -10^{-4}, with q' = 170 W/m, which roughly corresponds to the condition where the maximum $\Delta\Gamma$ is observed at $\lambda = 2\ \mu$m, and on a SF-PCF with the same pitch but $\Delta n = -2.10^{-4}$ at $q' = 340$ W/m, which is the maximum value of the heat load taken into account. The results have been compared with those obtained for a LPF with d/LPF = 0.20 with Δn = -2.10^{-4}, operating with q' = 340 W/m. The overlap difference for both SF-PCF slightly increases with the wavelength, with a variation of about 0.08 over the considered range. The SF-PCF operating at q' = 170 W/m shows a remarkable overlap difference close to 0.5 over the whole band, with maximum value of 0.54 at 2100 nm. Despite a lower $\Delta\Gamma$, also the SF-PCF operating at q' = 340 W/m is SM over the whole range, reaching Δn values between 0.33 and 0.4. These performances are better than those obtained by the LPF for the same heat load, being its overlap difference close to the threshold for SM operation at $\Delta\Gamma$ = 0.3 throughout the considered wavelength span.

3.5 Effective area

Fig.3.5(a) shows the effective area calculated at $\lambda = 2\ \mu$m for the LP_{01}-like mode of the SF-PCFs with the three considered values of core down-doping and $d/_{SFF} = 0.24$, as a function of the heat load. The curves have been drawn only for values of q'

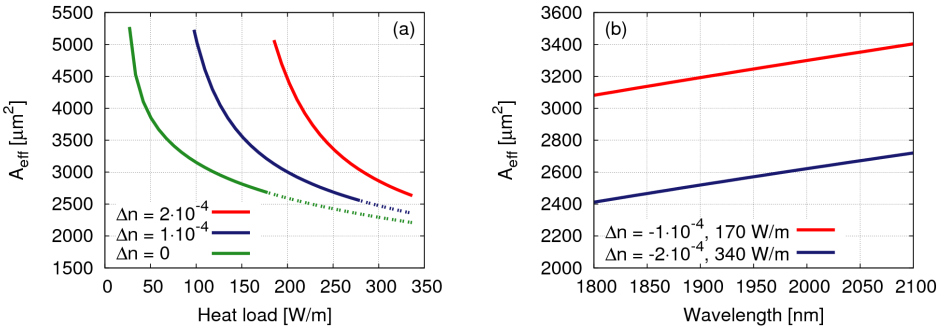

Figure 3.5: (a) Effective area of the SF-PCF with $d/\Lambda_{SFF} = 0.24$ and different values of core down-doping, calculated at $\lambda = 2$ μm as a function of the heat load. Dashed lines are used where fibers operate in multi-mode regime. (b) Effective area of the SF-PCF with $d/\Lambda_{SFF} = 0.24$ and $\Delta n = -2 \cdot 10^{-4}$ for a heat load of 340 W/m (red line) and of the SF-PCF with $d/\Lambda_{SFF} = 0.24$ and $\Delta n = -10^{-4}$ for a heat load of 170 W/m (blue line).

that ensure an overlap larger than 0.7, since lower values of Γ are not suitable for amplification, and are dashed where the fibers operate in multi-mode regime. The intense heating of the fiber has a remarkable effect on A_{eff} , roughly halving its value from about 5000 μm^2 to about 2600 μm^2 at the maximum heat load allowed for SM operation. Notice that down-doping does not affect these limits, but only determines the heat load at which these values of A_{eff} are obtained. For example, an effective area of 3000 μm is reached by the fiber without core down-doping at q' = 120 W/m, at q' = 200 W/m by the fiber with Δn = -10^{-4} and at q' = 280 W/m by the fiber with Δn = -2.10^{-4}. Notice also that the effective area shrinking due to heating is comparable to the values that have been found experimentally for the Tm-doped fiber laser based on the LPF with similar core diameter [44].

The effective area as a function of the wavelength of the two SF-PCFs already considered in Fig. 3(b), with the same heat load conditions previously used, is reported in Fig. 4(b). In both cases, the effective area change with the wavelength has a similar slope, with an increase over the considered wavelength range of about

$350\mu m^2$. When the maximum mode discrimination is achieved, that is by the fiber with Δn = -10^{-4} at q' = 170 W/m, A_{eff} is between 3100 μm^2 at λ = 1800 nm and 3400 μm^2 at λ = 2100 nm. On the other hand, by considering the fiber with Δ n = -2.10^{-4} at q' = 340 W/m, an effective area between 2400 μm^2 at λ = 1800 nm and 2700 μm^2 at λ = 2100 nm is found.

Chapter 4

Circular Tubes Lattice Fiber

4.1 Introduction

Hollow-core fibers (HCFs) have been studied and developed for several decades. HCF consists of an optical-guiding central air-core surrounded by an arrangement of dielectric tubes running along its length. HCF is extremely helpful in reducing the propagation loss and absorption loss. HCF provides a new platform for light-gas interaction study [46] and applications where material properties are a limiting factor such as high power laser pulse delivery [47], mid, far-infrared and THz transmission [48],[49]. There are two main families of HCF based on their guidance mechanisms. The first HCF family guides via photonic band-gap (PBG) [24]. The PBG fiber holds the potential for guiding light with attenuation theoretically lower than the fundamental limit of $\sim$0.15 dB/km in conventional optical fibers [13], however it exhibits a limited optical bandwidth. The other HCF family is still attracting for an intense study and technological development, relies for guidance on a combination of inhibited coupling to low density of states cladding modes and anti-resonance [46]. This family of HCF is distinguished by its broadband optical guidance and the relatively higher transmission loss-levels compared to the PBG guiding HCF. Fibers belong to this family are called by Inhibited Coupling Fibers.

Circular Tube Lattice Fibers (CTLFs) are a particular kind of Inhibited Coupling

Fibers composed of a ring of tubes surrounding a hollow core [50]. The low overlap of a travelling power with the dielectric composing the tubes makes these fibers good candidates for the transmission in the spectral ranges where low loss dielectrics are not available. Several examples have been demonstrated both in infrared [51], [52] and THz regions [2]. Cores greater than the wavelength are usually used in order to reduce as much as possible the propagation loss. Big cores allow to reduce both confinement loss (CL) and absorption loss (AL) being the latter proportional to the field-Dielectric Overlap (DO). However multi-wavelength cores make this kind of fibers big and hardly flexible. The knowledge of scaling laws correlating loss, working frequency, and core size could be very useful for an optimized design of them.

In this chapter the relationship between fiber loss, working frequency and core size in the CTLFs are numerically analyzed. The analysis of the confinement loss of the fundamental mode HE_{11} versus the working frequency and the core size is a classical problem in literature and it has already been addressed for various hollow core waveguides [53], showing different dependence for different kind of fibers. Numerical results show that CL exhibits a stronger dependence with respect to other hollow core fibers such as an air hole immersed in infinite dielectric medium [54], a single dielectric tube [55], and kagome fibers [56]. The AL dependence is weaker and it can be the dominant contribution in overall loss for small core size. The small fiber diameter of CTLF will be presented as a low-loss THz waveguiding.

4.2 Waveguiding Mechanism in CTLF

In CTLFs the hollow core is obtained by arranging N dielectric tubes in a circular pattern. Fig.4.1(a) shows the cross section of CTLFs and structure parameters. The tubes have dielectric refractive index n_H, thickness t, outer radius r_{ext}, core radius R_{co} and fiber diameter D. The background material is air. The fiber size depends on the number and size of tubes:

$$R_{co}(N, r_{ext}) = r_{ext}[\frac{1}{sin(\frac{\pi}{N})} - 1] \tag{4.1}$$

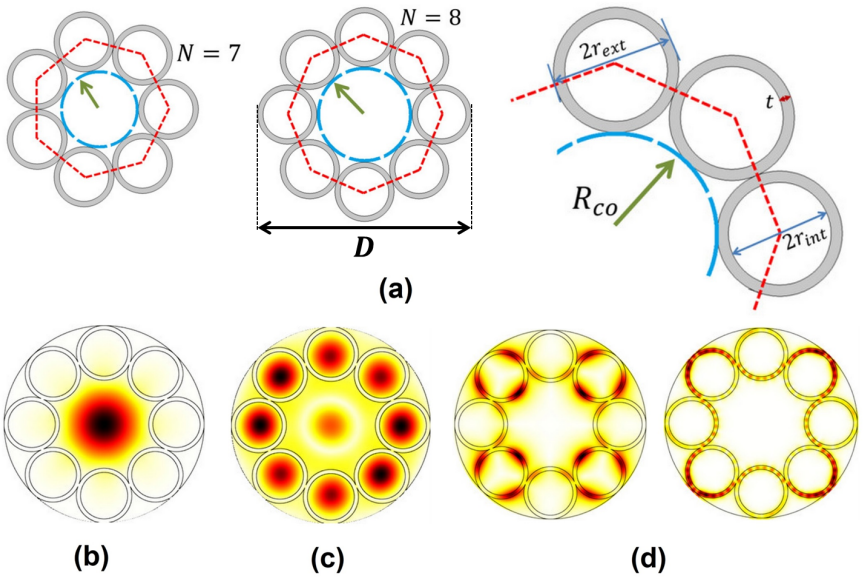

Figure 4.1: Circular tube lattice fiber (a) geometries, (b) Core Mode, (c) Cladding hole mode, and (d) dielectric modes with low (left) and high azimuthal dependence (right).

$$D = 2r_{ext}[\frac{1}{sin(\frac{\pi}{N})} + 1] \tag{4.2}$$

CTLFs support three different kinds of modes shown in Fig.4.1(bottom): core modes, which confine the major part of their electromagnetic power inside the core region; cladding hole modes, mainly confined in the inner part of cladding tubes; and cladding dielectric modes, mainly confined in the dielectric material [50]. The first two kinds of modes have effective index n_{eff} lower than air, whereas the latter has $1 < n_{eff} < n_H$. Conversely to PBG Fibers, in CTLF cladding supports modes at any given wavelength. The waveguiding is guaranteed by the inhibited coupling (IC) between core modes and cladding modes. Such coupling depends on two factors: the difference between the effective indices, and the field integral overlap. The effect of the former is maximized at the crossing point between the dispersion curves of the two involved modes (phase-matching condition). Since the fibers work in the large core regime, the effective index of the core mode is very close to 1, thus the frequencies of the phase-matching condition can be well approximated by the cut-off of the cladding dielectric modes. The second factor, the mode overlap, depends on spatial variation of the cladding dielectric modes on the transverse plane: the faster the variation, the lower the coupling.

Fig.4.2 shows the confinement loss (top) and dispersion curve (bottom) of the fundamental mode (FM) HE_{11} if a CTLF designed for THz applications, with $N = 8$, $r_{ext} = 0.873$ mm, and $t = 0.131$ mm, $n_H = 1.5207$ (Zeonex at 1 THz). The confinement loss shows an alternation of high and low loss regions. The bottom of the figure shows the dispersion curve of the fundamental core mode. Inside low loss regions, dispersion curve is well approximated by Marcatili's formula:

$$n_{eff}^M = 1 - \frac{1}{2}(\frac{u_{11}c}{2\pi f R_{co}})^2 \tag{4.3}$$

where u_{11} is the first root of the equation $J_0(u) = 0$. High loss regions and anticrossing in the dispersion curve fall at integer values of the normalized frequency [50]:

$$F = \frac{2t}{c}\sqrt{n_H^2 - 1}f \tag{4.4}$$

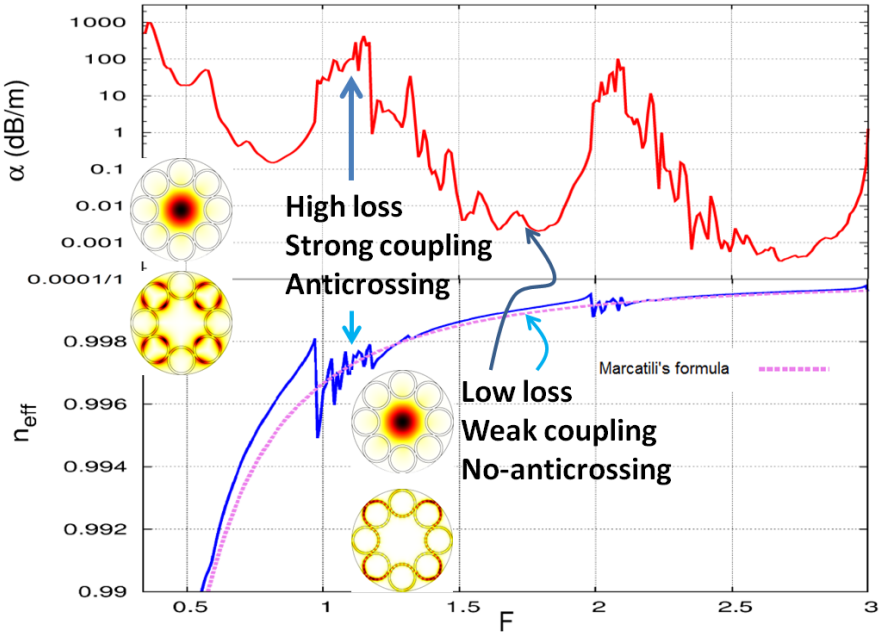

Figure 4.2: Confinement loss (top) and effective index (bottom) of the HE_{11} FM of CTLF with $N = 8$, $t = 0.131$ mm. Approximate of the FM, obtained with Marcatili's formula in Eq. (4.3), is also shown.

where c is the speed of light in vacuum, and f the absolute frequency. These frequencies correspond to the cut-off of the low azimuthal dependent dielectric modes of a single tube [50]. Between two consecutive high loss regions, there are only the cut-offs of high spatial dependent cladding modes and the coupling is strongly inhibited resulting in lower power leakage. These spectral regions will be called transmission windows (TWs). The spectral width of the high loss regions and thus the TWs, also depends on the ratio between inner and outer radius of the tubes composing the cladding and can be expressed as:

$$\rho = 1 - \frac{t}{r_{ext}} \tag{4.5}$$

4.3 Losses in CTLFs

The losses in CTLF can be generally divided into the confinement loss (CL) and absorption loss (AL). Confinement loss or leakage loss properties strongly depend on the electromagnetic field confinement mechanism and can be expressed by:

$$CL = 8.686\frac{2\pi f}{c} Im(n_{eff})[\frac{dB}{m}] \tag{4.6}$$

where $Im(n_{eff})$ is the imaginary part of the effective index of the fundamental core mode.

The absorption loss takes into account the fraction of the power carried on by the mode which is absorbed by the material composing the fiber. By assuming that the absorption due to the air is negligible, the AL depends on the material and the dielectric overlap (DO) according to [57][58]:

$$AL = \sqrt{\frac{\varepsilon_0}{\mu_0}} n_d \alpha_d DO, \tag{4.7}$$

where

$$DO = \frac{\int_{A_d} |E|^2 dA}{\int_A S_z dA} \tag{4.8}$$

being α_d the absorption loss of the dielectric bulk material, ε_0 and μ_0 the permittivity and the permeability in vacuum, respectively, E the electric field, S_z the z-component

of the Poynting vector, A_d the total area of cladding dielectric tubes, and A the total area of the fiber cross section. Dielectric overlap depends mainly on the fiber structure parameters such as tube thickness, tube number, and tube size.

Fig.4.3(bottom) shows that the absorption loss has the similar profile with the confinement loss which constitutes an alternation between high loss regions and low loss regions. The absorption losses in the high loss regions are much higher due to the strong coupling of the fundamental core mode with the cladding modes which affect higher value of dielectric overlap.

4.4 CTLFs Scaling Law

The analysis of scaling laws correlating loss, working frequency and core size is essential for the fiber design optimization. The scaling laws both CL and AL are essential to determine the best trade-off between low loss and small fiber diameter.

According to other kinds of hollow core fibers, the CL scaling law might be expressed as:

$$CL \propto \frac{1}{R_{co}^{p} f^{q}},\ p,q \in N^{+} \tag{4.9}$$

where p, and q are generic coefficients that must be determined.

The absorption loss depends on tube material (n_d, α_d) and dielectric overlap. The latter exhibits a very weak dependence on material whereas it strongly depends on the fiber geometry. For this reason we focused our analysis on the dielectric overlap scaling law instead of the absorption loss. The dielectric overlap scaling law might be expressed as:

$$DO \propto \frac{1}{R_{co}^{m} f^{n}},\ m,n \in N^{+} \tag{4.10}$$

where m and n are generic coefficients that must be determined.

4.4.1 Confinement Loss Scaling Law in CTLFs

The CL confinement loss for the fundamental core mode to a variation in the core size and working frequency has been addressed for various hollow core fibers. Confinement loss scales with $R_{co}^{-3} f^{-2}$ for an air hole surrounded by an infinite dielectric

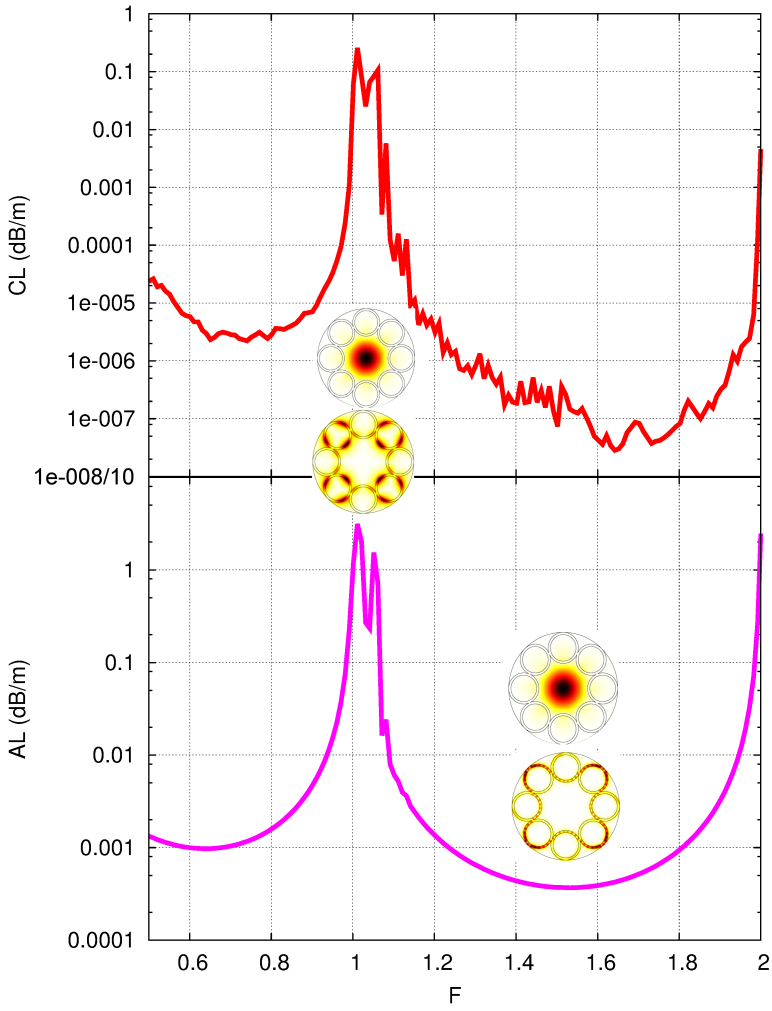

Figure 4.3: The confinement loss (top), and absorption loss (bottom) spectra. CTLF with r_{ext} = 6.549 mm, t = 0.131 mm, n_H = 1.5207 (Zeonex), N = 8.

medium [54]. In single tube fiber confinement loss scales with $R_{co}^{-4} f^{-3}$ [55], whereas it scales with $R_{co}^{-3} f^{-3}$ in case of Kagome fibers [56].

Confinement loss of the CTLFs depends on tubes parameters. High loss region bandwidth is inversely proportional to the ρ parameter. By reducing ρ, high loss regions spread affecting low loss region bandwidths and their local minima. Consequently, in order to investigate the CL and DO dependence on R_{co} and f, the ρ parameter must be kept constant. Fig.4.4 shows the CL of CTLFS with different value of ρ of the fibers with the same tube thickness t. The bigger value of ρ means the bigger tube size, and this affects lower width of the high loss regions. The depen-

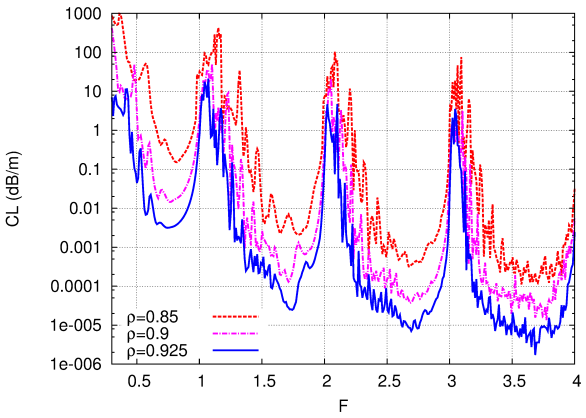

Figure 4.4: The comparison of the spectral width of high CL regions of the fibers with different ρ parameter, same tube thickness of $t = 0.131$ mm, $N = 8$.

dence of Scaling Law with R_{co} is evaluated by increasing number of tubes, N, and keeping ρ constant. As r_{ext} constant, according to Eq. (4.1), the R_{co} depends only on N parameter. Fig.4.5 shows the four windows of CL of the CTLF with $r_{ext} = 0.873$ mm, and $t = 0.131$ mm with $N = 6$-14. Core size, R_{co}, increases as N increases. In the third TWs, the difference between the minima of CL of $N = 6$ and $N = 14$ is almost three decades. The CL depends also on frequency. As the frequency increases, the CL decreases. By passing from I to IV transmission band the minima of CL at $N = 14$ reduces more than three decades.

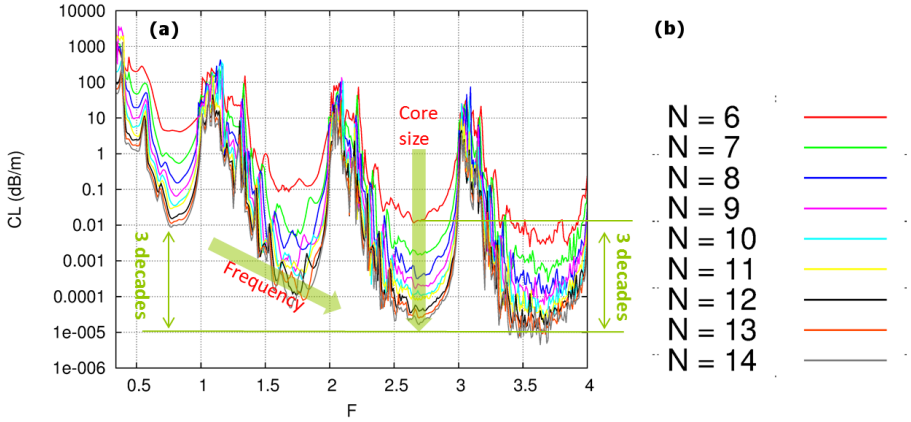

Figure 4.5: The dependence of CL to R_{co} and frequency (a) and the graph legend (b). The CTLF parameters: t = 0.131 mm, r_{ext} = 0.873 mm, N = 6-14.

CL depends on geometrical parameters such as the tube thickness and tube size. Fig.4.6(a) shows the CTLF with $N = 8$, $t = t_0 = 0.131$ mm. Maintaining the tube thickness but using bigger cladding tubes, in this case $r_{ext2} = 2r_{ext1}$ as shown in Fig.4.6(b), the spectral width of high CL regions become smaller. CL is lower as a result of bigger core radius. Fig.4.6(c) shows the CTLF with the same r_{ext}, thus the same core radius, but with the smaller tube thickness. From the spectrum, it is shown that the spectral position of high loss regions are shifted to the right. In the case of higher tube thickness, the high CL loss regions would be shifted to the left. In order to determine the value of p and q, frequency and core radius dependencies have been separately investigated and have considered the geometrical parameters.

In Fig.4.7(a)-(b) confinement loss versus normalized frequency of two CTLFs with t = 0.131 mm, r_{ext} = 0.873 mm, n_H = 1.5207 (Zeonex) and N = 8, N = 12 respectively are reported. The dashed line fitting curves of the minimum loss inside TWs with Eq. Kf^{-q}, being K an arbitrary constant. By increasing the number of tubes from N = 8 to N = 12 the core size increases and the loss decreases. Fig.4.7(c)-(d) show the confinement loss spectra of a similar CTLFs with larger tubes composing the cladding, having r_{ext} = 1.747 mm. Notice that the confinement losses are reduced

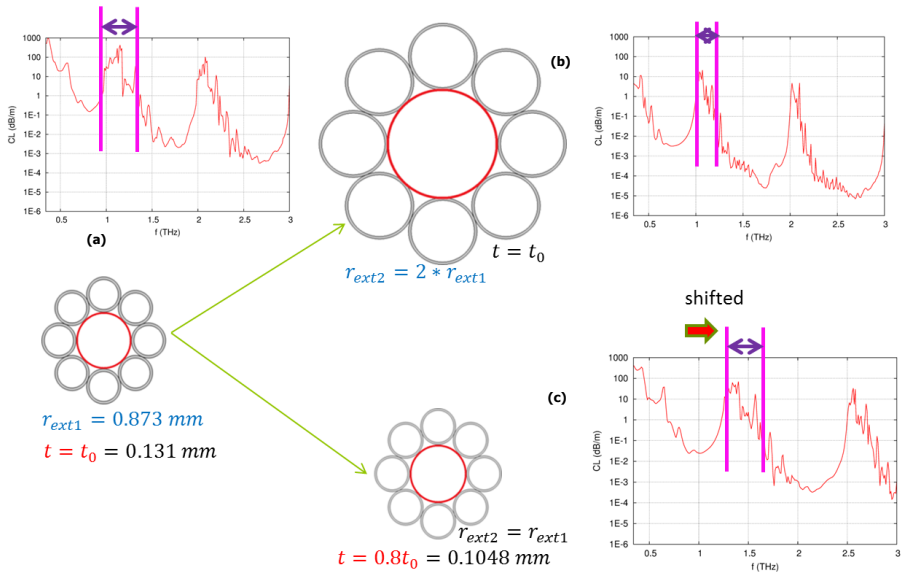

Figure 4.6: The dependence of CL to CTLF parameters. The CTLF with $N = 8$ with difference fiber parameters (a) tube thickness $t = 0.131$ mm, $r_{ext} = 0.873$ mm, (b) $t = 0.131$ mm, $r_{ext} = 1.747$ mm, and (c) $t = 0.1048$ mm, $r_{ext} = 0.873$ mm.

by about two orders of magnitude with respect to those shown in Fig.4.7(a)-(b). Finally, Fig.4.7(e)-(f) consider a couple of CTLFs with the same parameter of those Fig.4.7(a)-(b) but with thinner tubes, being $t = 0.1048$ mm. Since the high loss frequencies depends on tube thickness through Eq. (4.4), the thinner tubes push high loss peaks toward higher values of frequency f and once more loss reduces with respect to Fig.4.7(a)-(b). Considering the variation of all geometrical parameters of CTLFs (number of tubes, tube radius, and tube thickness) as shown in Fig.4.7, the numerical results show a good agreement between the minimum values of the confinement loss in the TWs and the fitting curve with $q = 4.5$.

Previous results show that for a given frequency, CL also depends on geometrical parameters like tube size r_{ext} and thickness t. In order to consider only the dependence on the core size, different fibers with the same geometrical tube characteristics have been considered. Since core size also depends on number of tubes through Eq. (4.1), fibers composed by the same tube type but with different number of tubes N from 6 to 14 are here considered. Left and right column of Fig.4.8 shows that the CL versus the core radius (i.e. different number of tubes), of CTLFs with different geometrical parameters computed at two different normalized frequencies $F = 0.75$, and $F = 2.75$ respectively, corresponding to the minima in the first and third transmission window. The dashed lines show the curve KR_{co}^{-p} with K an arbitrary constant. In all cases, the values of CL are well fitted by the curve with $p = 4.5$. An exception is the case of $N = 6$ where CL is higher than the prediction of scaling law. This could be due to the extra coupling between the fundamental core mode HE_{11} and the cladding hole modes [50]. In fact, for $N = 6$ the core size is very close to the hole size of the tubes resulting in a phase matching condition between the aforementioned modes. For $N > 6$, the core size is significantly bigger than tube holes and the effective indices differ enough to make this kind of coupling negligible. Fig.4.9(a) shows the effective indices of core mode and cladding hole mode for $N = 6$, while Fig.4.9(b) shows the same curves for $N = 7$. The value of effective index of cladding hole mode is closer with the one of core mode for $N = 6$ than $N = 7$. From the inset figures of magnetic field distribution of $N = 6$, the core size is similar to the tube size results a phase matching condition between the Core Mode and the Hole Mode. It can be evidenced

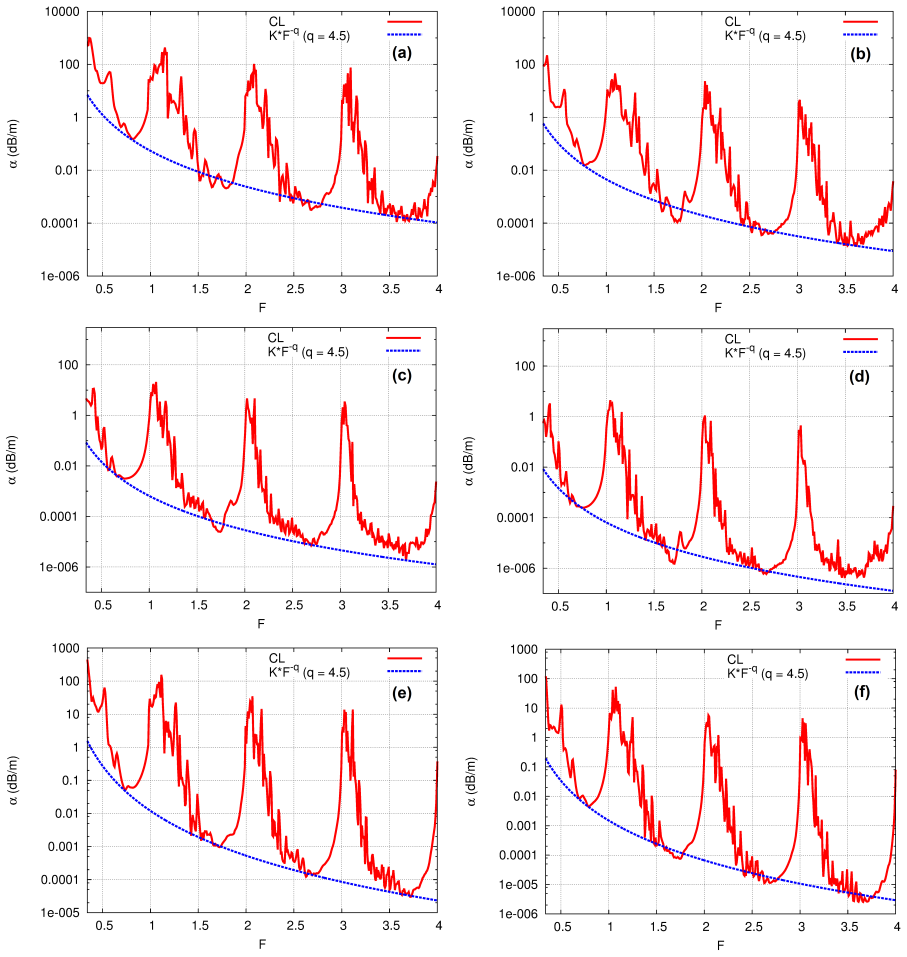

Figure 4.7: Confinement loss versus F and fitting curve of frequency for three different geometrical parameter of CTLFs (number of tubes, tube radius and tube thickness). Top: t = 0.131 mm, r_{ext} = 0.873 mm. Middle: t = 0.131 mm, r_{ext} = 1.747 mm. Bottom: t = 0.1048 mm, r_{ext} = 0.873 mm. Left column N = 8, right column N = 12. Best fitting curve of frequency with q = 4.5

by the existence of magnetic field distribution in the core region of the cladding hole mode.

Fig.4.10 shows the normalized CL of CTLF in Fig.4.5 by applying the R_{co} factor (p) and the frequency factor (q) both equal to 4.5. The figure shows that minima of CL in TWs are constant despite of core size and frequency, except for $N = 6$ which the minima of CL does not fit and higher than prediction.

4.4.2 Dielectric Overlap and Absorption Loss Scaling Law in CTLFs

The AL scaling law can be represented by the scaling law of dielectric overlap (DO) in Eq. (4.10). Fig.4.11(left) shows the dielectric overlap versus F of the CTLF analyzed in the previous section taken only for the first two TWs, for different geometrical parameters t and r_{ext} as well as number of tubes N is reported. The CTLFs here considered have different high loss frequencies and core size according to Eq. (4.1) and (4.4). Despite the geometrical parameter, the numerical results show that by using the value $m = 3$ and $n = 2$ the curves of absorption loss scaling law in Fig.4.11(right) for corresponding fibers are almost overlapped for all values of N.

Fig.4.12 shows the DO (left) and normalized DO (right) of three different CTLFs in four transmission windows taken for number of tubes N = 6,8,10, and 14. Despite of the fiber geometrical parameters the DO scaling law has a good agreement with $m = 3$ and $n = 2$ for a whole transmission windows. Although AL also depends on dielectric absorption coefficient and thus on the material used to make the fiber, this weaker dependence can potentially make the AL the main limiting factor in reducing the total propagation loss of CTLF in mid infrared and THz spectral regions, where material absorption plays an important role. Results show that in this kind of fiber the dielectric overlap and the absorption loss have weaker dependance on the core radius and the frequency with respect to the confinement loss.

4.5 Reduced CL with nested ring

Nested small rings are added with the same thickness as the outer ones and attached to the cladding at the same azimuthal position, as shown in Fig.4.13. Fig.4.14 shows the

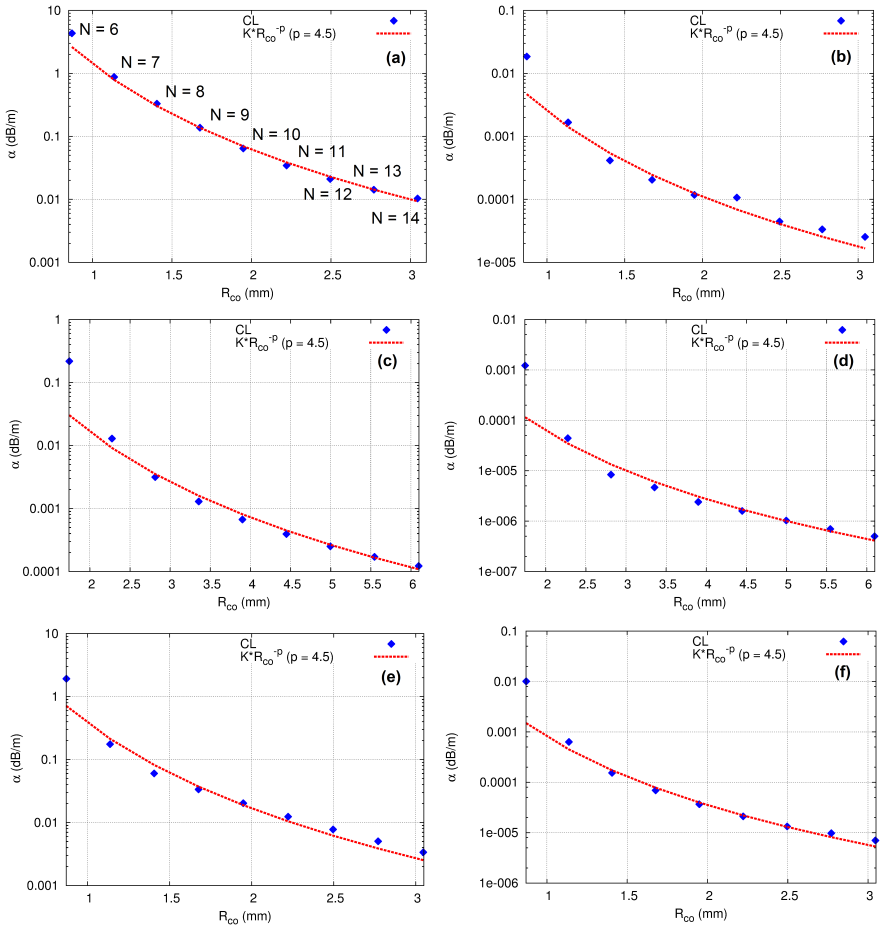

Figure 4.8: Confinement loss versus R_{co} and fitting curve $KR_{co}^{-4.5}$ for three different geometrical parameter of CTLFs at F = 0.75 (left column) and F = 2.75 (right column). Top: t = 0.131 mm, r_{ext} = 0.873 mm. Middle: t = 0.131 mm, r_{ext} = 1.747 mm. Bottom: t = 0.1048 mm, r_{ext} = 0.873 mm.

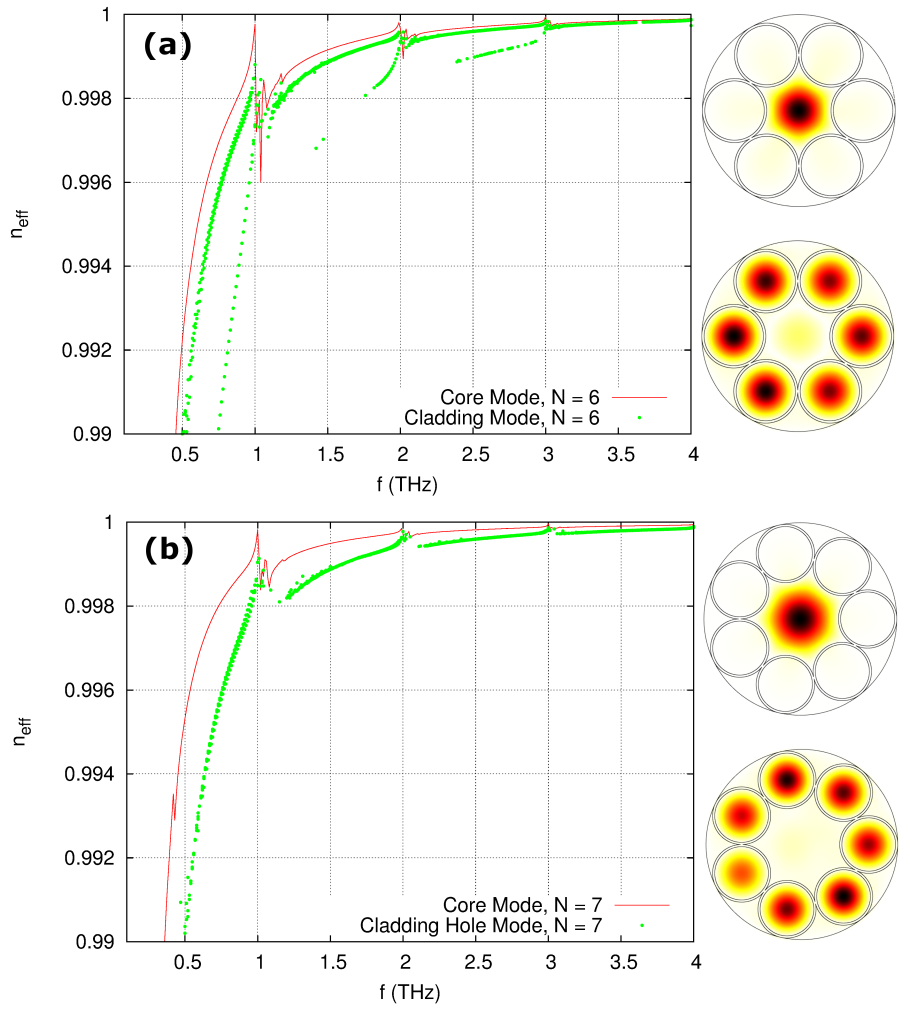

Figure 4.9: The comparable fiber core size and tube size causes a phase matching condition between the Core Mode and the Hole Mode of CTLF with $N = 6$ (top) while for $N = 7$ (bottom) not evident.

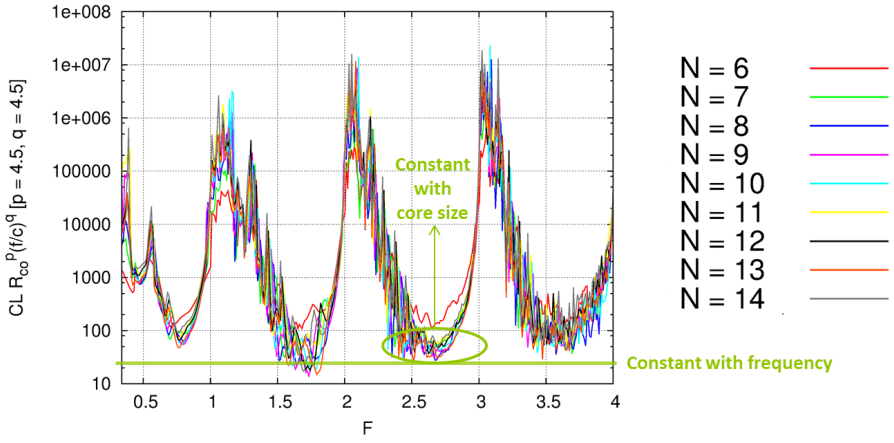

Figure 4.10: The normalized CL of CTLF with t = 0.131 mm, r_{ext} = 0.873 mm.

numerical analysis for CL and DO of the CTLF with nested ring. From Fig.4.14(left), reduction in CL can be achieved by adding nested ring within the tube cladding. For example the reduction of minimum CL is more than 10 times in the second transmission windows, despite the number of tubes while in the first transmission windows the CL reduction is small. In the previous CTLF design (without nested small ring), the field associated with the fundamental core mode is not completely confined within the hollow core, but extends beyond the dielectric core boundary into the cladding holes. By adding an additional ring within the cladding holes of the fiber, light can be excluded from this area giving an improved confinement to the fiber core, results of the reduction of the confinement loss. In principle, further reduction in the confinement loss can be achieved by adding extra rings within the fiber cladding [59], for example by adding two nested rings in the dielectric tube. The dielectric overlap of the core mode is a critical parameter as it influences the absorption loss which can be a lower bound in the total fiber loss. As we can see, despite adding additional nested dielectric ring to the structure, the minimum dielectric overlap of the guided mode remains almost exactly the same as shown in Fig.4.14(right).

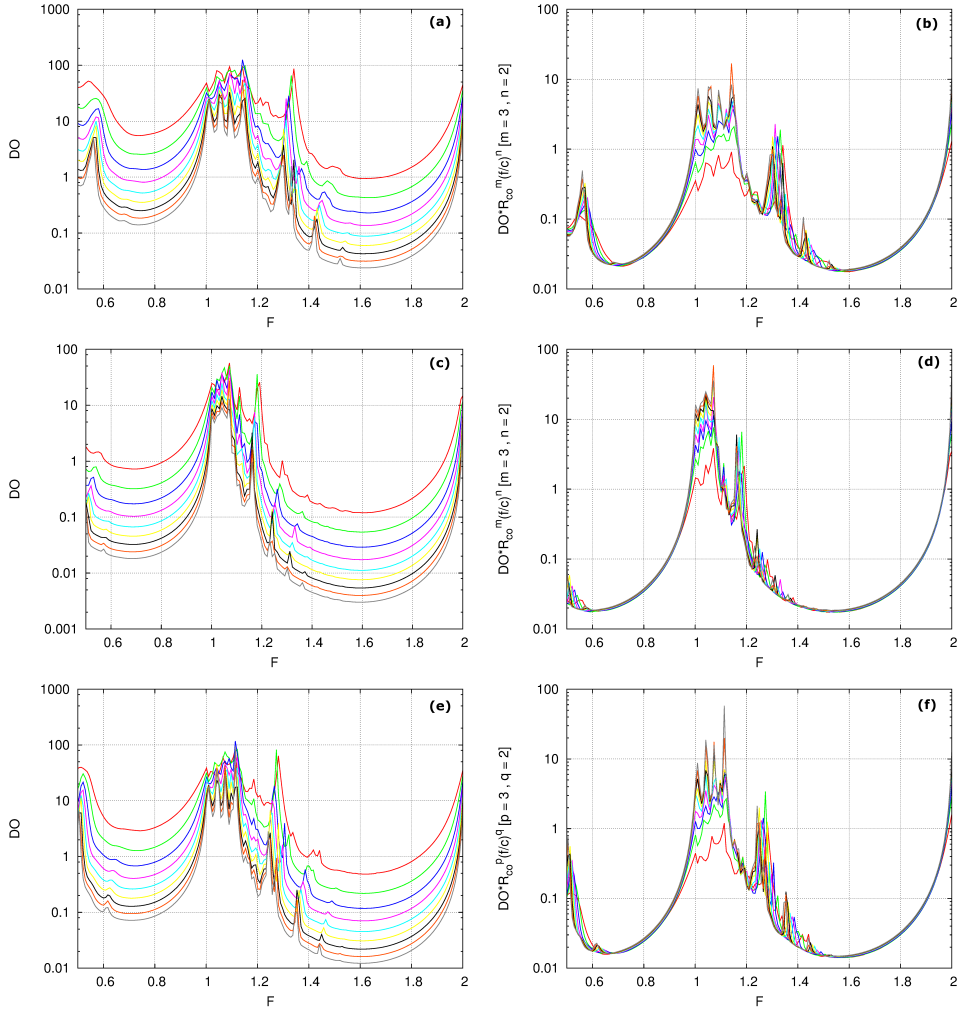

Figure 4.11: Dielectric overlap (left) and Dielectric overlap scaling law (right) for three different geometrical parameter of CTLFs. Top: t = 0.131 mm, r_{ext} = 0.873 mm. Middle: t = 0.131 mm, r_{ext} = 1.747 mm. Bottom: t = 0.1048 mm, r_{ext} = 0.873 mm. The graph legend refers to Fig.4.5(b).

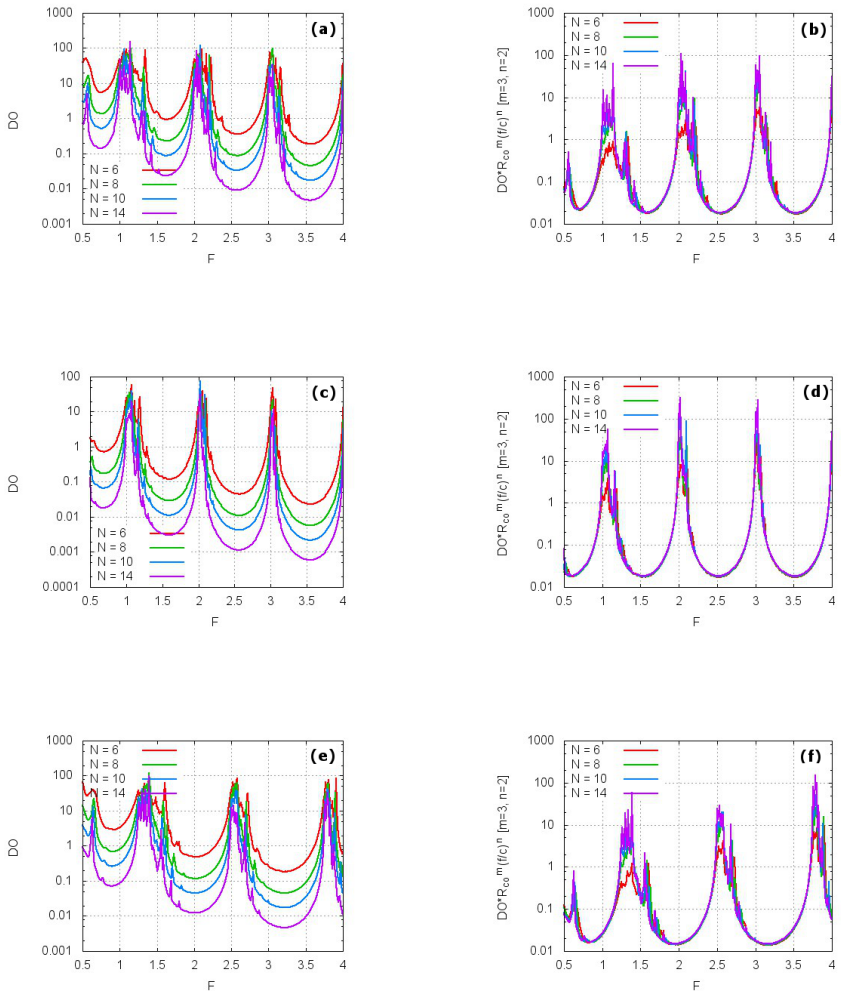

Figure 4.12: The four transmission windows of Dielectric overlap (left) and Dielectric overlap scaling law (right) for three different geometrical parameter of CTLFs. Top: t = 0.131 mm, r_{ext} = 0.873 mm. Middle: t = 0.131 mm, r_{ext} = 1.747 mm. Bottom: t = 0.1048 mm, r_{ext} = 0.873 mm.

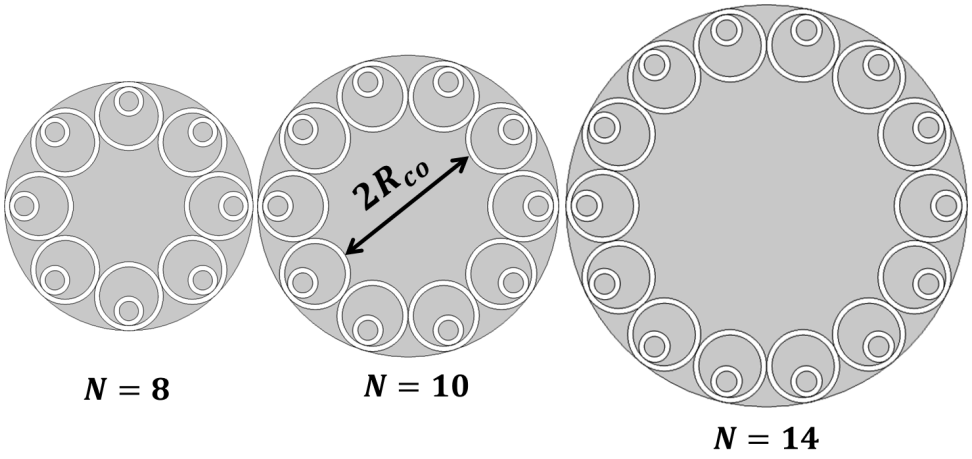

Figure 4.13: CTLF structure with nested ring with example of N = 8, N = 10, and N = 14.

4.6 CTLF for THz Transmission

In terahertz application, development of fibers with low loss, broad transmission band and high free space coupling efficiency is still a hot and key issue [49][60]. The challenge in waveguide development is THz frequencies is poor characteristics of both metal and dielectrics in this frequency region [61]. Metal, a good waveguide material in radio frequency and microwave range exhibits high loss from the finite conductivity in THz frequencies. Dielectrics waveguides are flexible and with circular cross sections, they are most used in optical frequencies, but in THz frequencies dielectric waveguides suffer from high material absorption. Considering that dry air is almost transparent for THz wave propagation, hollow core (HC) fibers are extremely helpful in reducing the propagation loss because only a small fraction of electromagnetic power propagates in dielectric material. HC-CTLFs have proposed for a flexible low loss THz waveguide [2]. They consist of a hollow core surrounded by a circular arrangement of dielectric tubes. Dielectric tubes are in turn surrounded by a heat-shrink jacket that allows the fiber to be flexible. The first prototypes made of polymethyl-

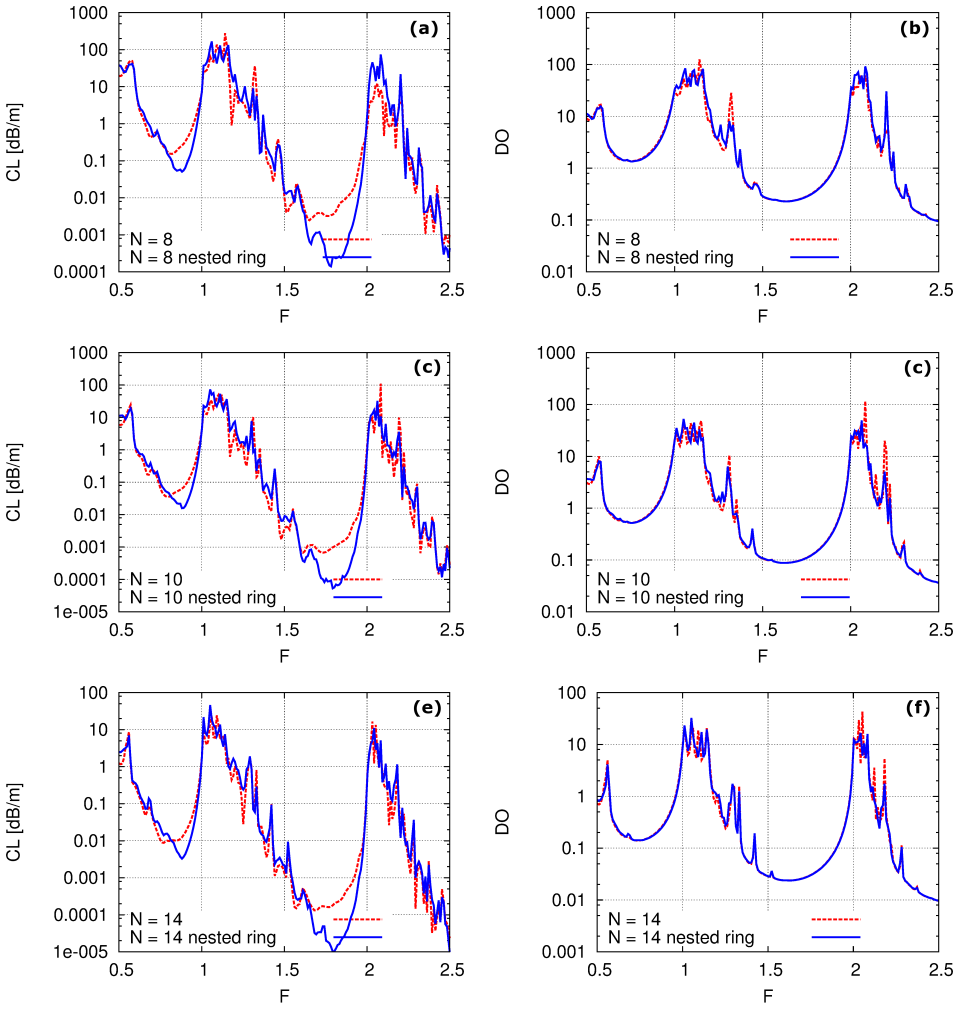

Figure 4.14: The CL (left) and DO (right) of CTLF with nested small ring. Tube thickness for outer and nested rings $t = 0.131$ mm, external radius of outer ring $r_{ext} = 0.873$ mm. Top: $N = 8$, Middle: $N = 10$, Bottom: $N = 14$.

methacrylate tubes have shown that propagation loss can be significantly reduced with respect to the bulk material one over a wide spectral range. Moreover high coupling coefficients, up to 95 %, can be obtained with a free space Gaussian beam [62]. However, in order to reduce confinement loss and absorption loss large core fibers are usually used. Since the wavelength at terahertz regime is of some hundreds of micrometers, this can significantly increase the fiber size and reduce its flexibility. Consequently, a trade-off between low loss and small dimension is mandatory.

The CTLF design for flexible low loss waveguide for THz will be discussed. The fiber is designed to work at the central frequency 1 THz with a diameter of 5 mm as considered small enough to support a flexible waveguide for THz operation. Beside that, in this fiber diameter, the minimum of absorption loss (AL) is relatively small (between 0.1 dB/m and 1 dB/m) and in the same order of magnitude with the minimum of confinement loss (CL). In the first step, the thickness of the tube have been fixed to 100 μm for all number of tubes, thus the transmission windows position are fixed despite of the number of tubes. This tube thickness is obtained by setting the central frequency at 1 THz. We will investigate the fiber parameters (number of tubes, thickness) that are suitable to provide the optimum Transmission Windows. We will focus to investigate the first transmission where 1 THz is located in order to increase as much as possible the loss spectral region of the fiber. The first transmission band is roughly bounded between $F = 0.5$ and $F = 1.0$ with a minimum loss at $F = 0.75$ [50]. We will work in the absolute frequency f rather than the normalized frequency F to properly identify the optimum TWs at around 1 THz. As in practice, the length of the fiber used in THz application is around 1 m, the maximum loss of 1 dB/m has been considered sufficient to support the propagation of light in this fiber length. After obtaining the optimum TWs, the thickness can be optimized to obtain more bandwidth gain. Results show that by using the number of tubes, $N = 14$, the CTLF possesses the transmission window bandwidth around 280 GHz ranging from 0.94 THz to 1.22 THz. Further optimization can be performed by reducing the tube thickness to obtain the additional bandwidth in the higher frequencies but with the expense of loss of relatively small bandwidth in the lower frequencies.

4.6.1 Structures

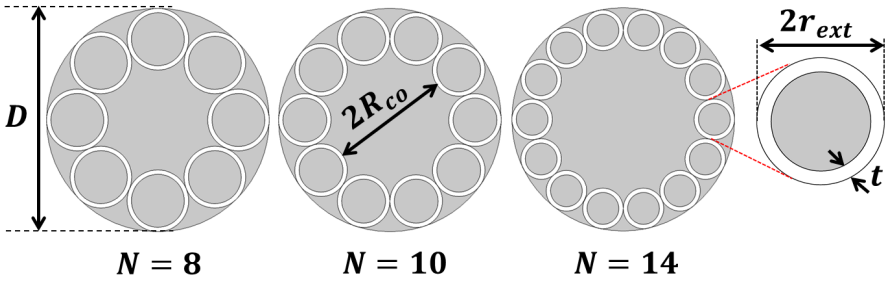

Figure 4.15: Circular tube lattice fiber (a) N = 8, (b) N = 14, and (c) N = 18.

Fig.4.15 shows the structures of designed CTLFs with the same fiber diameter D = 5 mm. The figure shows the example of cross-sections of CTLF with number of tubes N = 8, N = 14, and N = 18.The grey regions represent air and the white ones represent dielectric. All tubes have same outer diameter $2r_{ext}$, thickness t and refractive index n_H. The tubes composing the fiber are made of Zeonex with refractive index n_H = 1.5207 and bulk absorption coefficient α_m = 0.93 dB/cm at 1 THz. The number of tubes surrounding the core is changed in order to increase the core size without effecting the overall fiber diameter. The spectral widths depend on the ρ parameter. With the constant thickness, decreasing r_{ext} means reducing ρ that will cause the increasing of high loss region spectral widths [50]. As in CTLFs the core radius depends on number and size of tubes, by increasing number of tubes it is possible to increase core size without changing the fiber diameter D: $2R_{co} = M.D$, where $M = [1 - sin(\frac{\pi}{N})]/[1 + sin(\frac{\pi}{N})]$. Fig.4.16 shows the relation between core diameter ($2R_{co}$) and fiber diameter D ($2R_{co} = M.D$). As number of tubes N increases, the core diameter $2R_{co}$ increases within the constant fiber diameter D. For example, CTLF with N = 8 has the core diameter 0.45 times fiber diameter and CTLF with N = 18 has the core diameter around 0.7 of fiber diameter. Table 4.1 confirmed the situation by providing the numerical values. From the table it is evident that by increasing the tube numbers, the fiber will reduce the tube external radius r_{ext} but in the same time it will increase the core radius R_{co}.

Number of tubes	External tube radius, r_{ext} (in mm)	Core radius, R_{co} (in mm)
8	0.692	1.113
10	0.590	1.316
12	0.514	1.467
14	0.455	1.585
16	0.408	1.678
18	0.370	1.754

Table 4.1: CTLF Parameters for $D = 5$ mm, $t = 100$ μm.

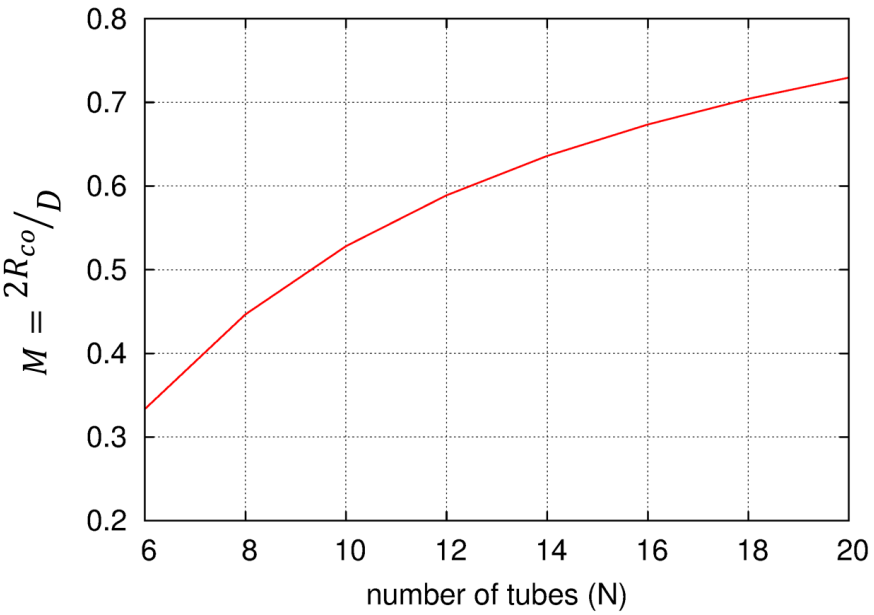

Figure 4.16: Factor of the increase of Core Diameter to the increase of number of tubes (M=$2R_{co}/D$).

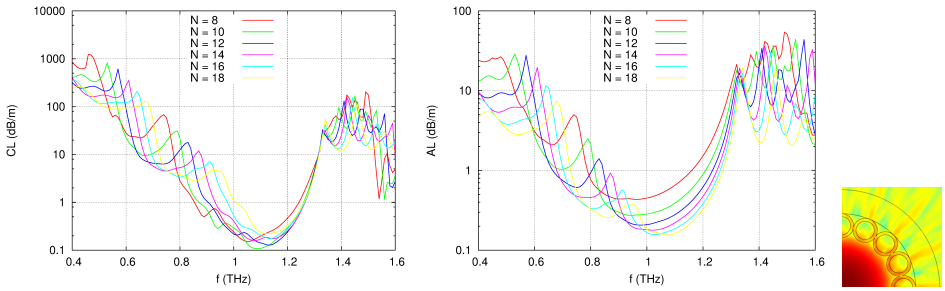

Figure 4.17: Confinement loss (left), absorption loss (right) of CTLF of Zeonex with fiber diameter $D = 5$ mm and tube thickness $t = 100\ \mu$m. Insert picture is the magnetic field modulus (power 0.1) for local peak spectrum for $N = 16$ at $f = 0.91$ THz.

4.6.2 Analysis

Fig.4.17 shows the CL and AL of CTLF for different number of tubes $N = 6$ - 14 (even). n and α_m frequency dependences have been taken into account by fitting the experimental values reported in [63]. The AL graphs are flatter than the corresponding CL ones. By increasing N AL reduces, while CL has difference properties. Having the greatest R_{co} CTLF with $N = 18$ has the maximum CL. CTLF with $N = 10$ has minimum CL, while $N = 8$, 12, and 14 CL are roughly constant. Since the AL is dominant with respect to CL, this will result in a total loss reduction. The reduction of ρ in the increasing of N is evident by a blue shift of peak both in CL and AL. In fact, by increasing N with D constant, the ρ parameter of the tubes reduces causing the blue shift of the cut-off frequencies of the cladding mode with the azimuthal number greater than one [50]. However the peak value reduces as N increases. The local peak is due to the coupling between the fundamental core mode and the dielectric tube mode that causes of fundamental core-mode leakage. The inset picture describes the local peak of the fiber with $N = 16$ and takes place at the frequency $f = 0.91$ THz.

Fig.4.18 shows the total loss of CTLF which is the sum of AL and CL. Notice that due to the dominant of AL, CTLF with $N = 18$ no longer has the maximum loss as in CL, but minimum along with $N = 16$ and 14. By choosing the a total reference

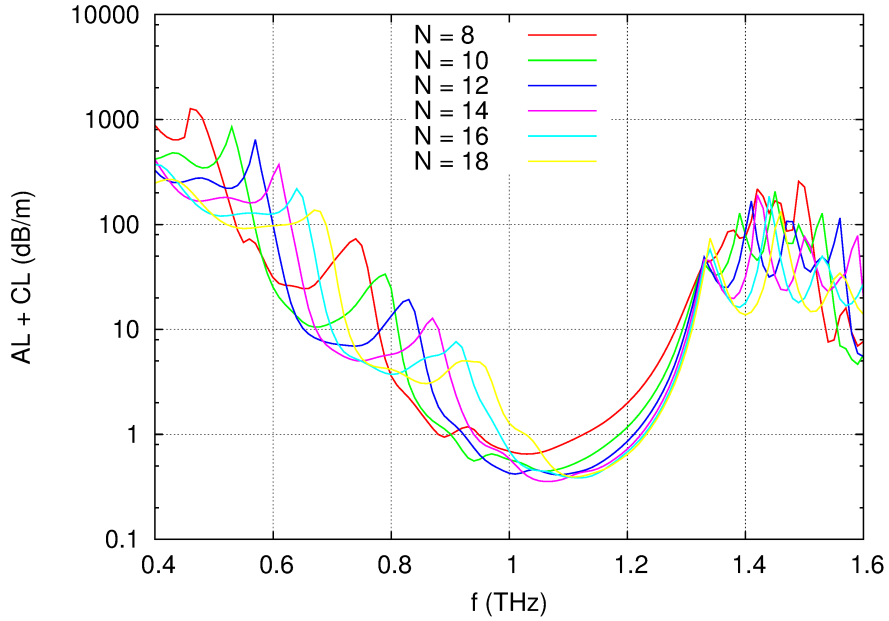

Figure 4.18: Total loss of CTLF of Zeonex with fiber diameter D = 5 mm and tube thickness t = 100 μm.

value of 10 dB/m, a remarkable transmission band of about an octave, ranging from 0.7 THz to 1.3 THz, is obtained with $N = 16$. Notice that the external fiber diameter is lower than 12 times the longest wavelength of the considered band. By reducing the reference loss value as low as 1 dB/m the maximum band of 280 GHz is obtained with $N = 14$, ranging from 0.94 THz to 1.22 THz.

Beside the number of tubes, further optimization can be performed by reducing the tube thickness. Fig.4.19, Fig.4.20, and Fig.4.21 show the CL, AL, and Total Loss of the CTLF with $N = 18$ with the thickness $t = 100$ μm and $t = 90$ μm. Reducing the thickness from $t = 100$ μm to $t = 90$ μm, from Fig.4.21, the transmission window gains the additional bandwidth for around 0.14 THz in the higher frequency (shifted to the right from the frequency of 1.29 THz in $t = 100$ μm into $f = 1.43$ THz in $t = 90$ μm). But, this gain of bandwidth obtained at the expense of the loss of bandwidth in the lower frequency, although it is only a small value for about 0.03 THz. This loss of TW bandwidth is due to the shift of the TW to the right from the minimum frequency of 0.74 THz of the fiber with $t = 100$ μm to $f = 0.77$ THz, which is the minimum frequency of CTLF with $t = 90$ μm.

4.6.3 Touchless cladding tubes

The CTLF design optimization for THz waveguiding has been performed by reducing the tube thickness. This approach obtained the significant gain of bandwidth in the higher frequency at the expense of the loss of bandwidth in the lower frequency. More than that, the local peak increases which might break off the TW bandwidth. The dash-dot line graphs of reduced tube thickness ($t = 90$ μm) in Fig.4.23 show the same phenomenon of the increasing of local peak when compared with the dashed lines of CTLF with $t = 100$ μm. The significant increase of local peak has been noted in the absorption loss for CTLF with $N = 16$.

Fig.4.22 shows the modification of CTLF structure. The tube thickness is $t = 90$ μm with the external tube radius has been kept constant according to the number of tubes, in this case $N = 14$ and $N = 16$ (see Table 4.1). By enlarging the core radius for about one thickness length, the cladding tubes are not touching each other. By modifying in this way, the core radius and fiber diameter become slightly larger, for

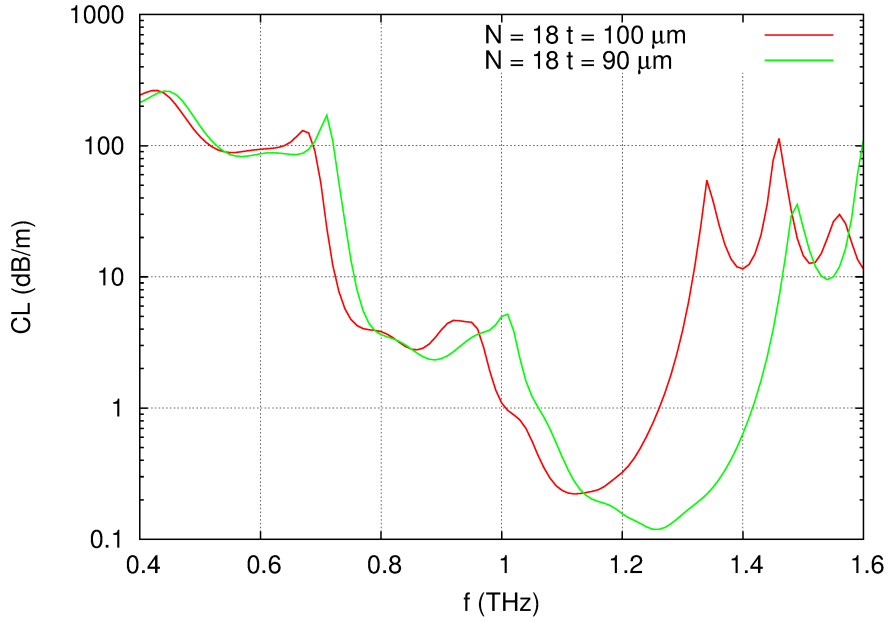

Figure 4.19: CL of CTLF with $N = 18$ with different tube thickness $t = 100\ \mu$m and $t = 90\ \mu$m.

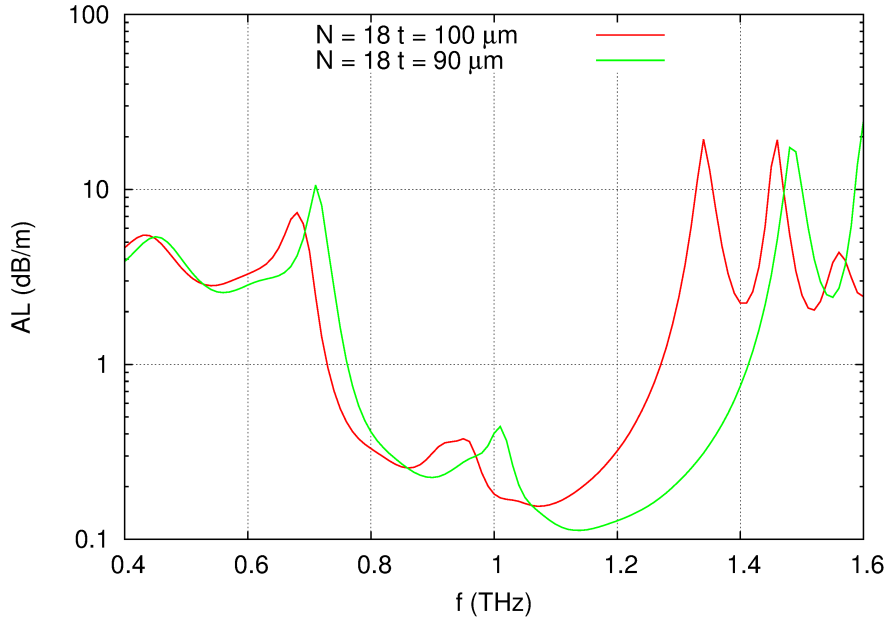

Figure 4.20: AL of CTLF with $N = 18$ with different tube thickness $t = 100\ \mu$m and $t = 90\ \mu$m.

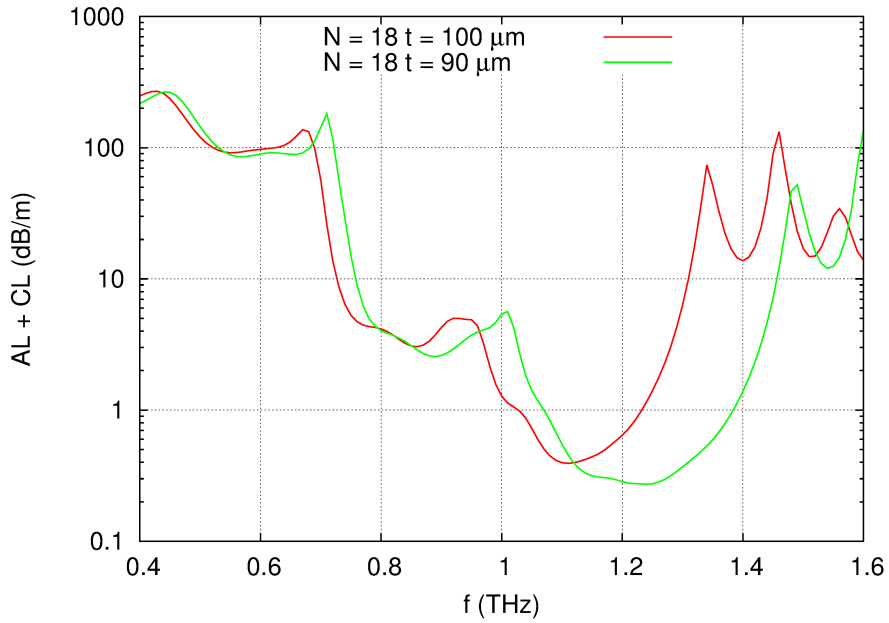

Figure 4.21: The gain of total loss of CTLF with $N = 18$ by reducing the thickness from $t = 100\ \mu$m to $t = 90\ \mu$m.

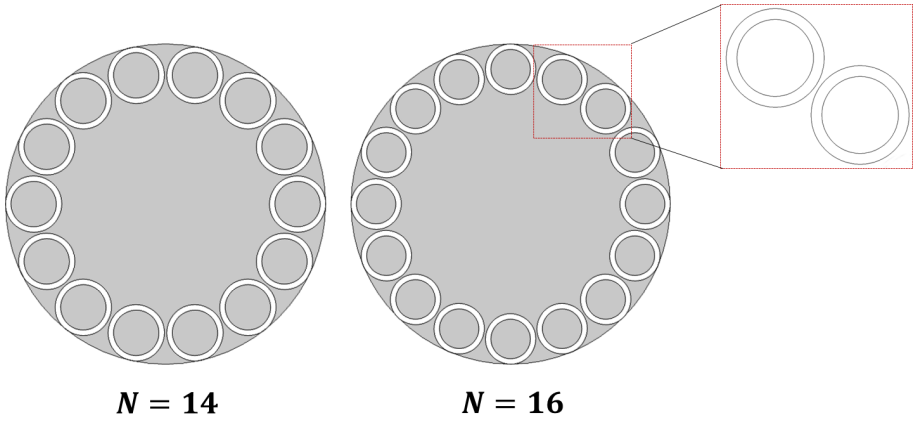

Figure 4.22: CTLF with touchless cladding tubes N = 14, R_{co} = 1.675 mm, D = 5.170 mm (left) and N = 16, R_{co} = 1.769 mm, D = 5.169 mm (right). Inset zoom picture shows that the neighbor cladding tubes do not touch.

example for N = 14, the fiber diameter changed from D = 5 mm to D = 5.170 mm.

The solid lines in Fig.4.23 describe the CL, AL, and Total Loss of CTLF with touchless cladding tubes for N = 14 (left) and N = 16 (right). Despite of the number of tubes, the local peaks decrease for CL, and AL refers to the dash-dot line. Refer to the only thickness reduction, the obtained transmission windows band of CTLF with touchless cladding tubes at N = 16 is the same for around 720 GHz range from 0.73 THz to 1.45 THz by applying the allowable loss of 10 dB/m. The touchless cladding tubes have the benefit of reduction of total loss, for example it achieved the minimum loss of 0.20 dB/m at 1.18 THz lower than 0.25 dB/m in only tube thickness reduction approach at the same frequency. Another clear benefit of CRLF with touchless cladding tubes is the reduction of local peak around 1.74 dB from 8.69 dB/m at 0.96 THz of dash-dot line to 6.95 dB/m at 0.93 THz. Here, the touchless cladding tubes combine with the reduction of tube thickness is preferable to obtain the optimum transmission band with lower fiber loss than only tube thickness reduction approach.

Taking the allowable loss of 1 dB/m, for N = 14, here we don't take the benefit

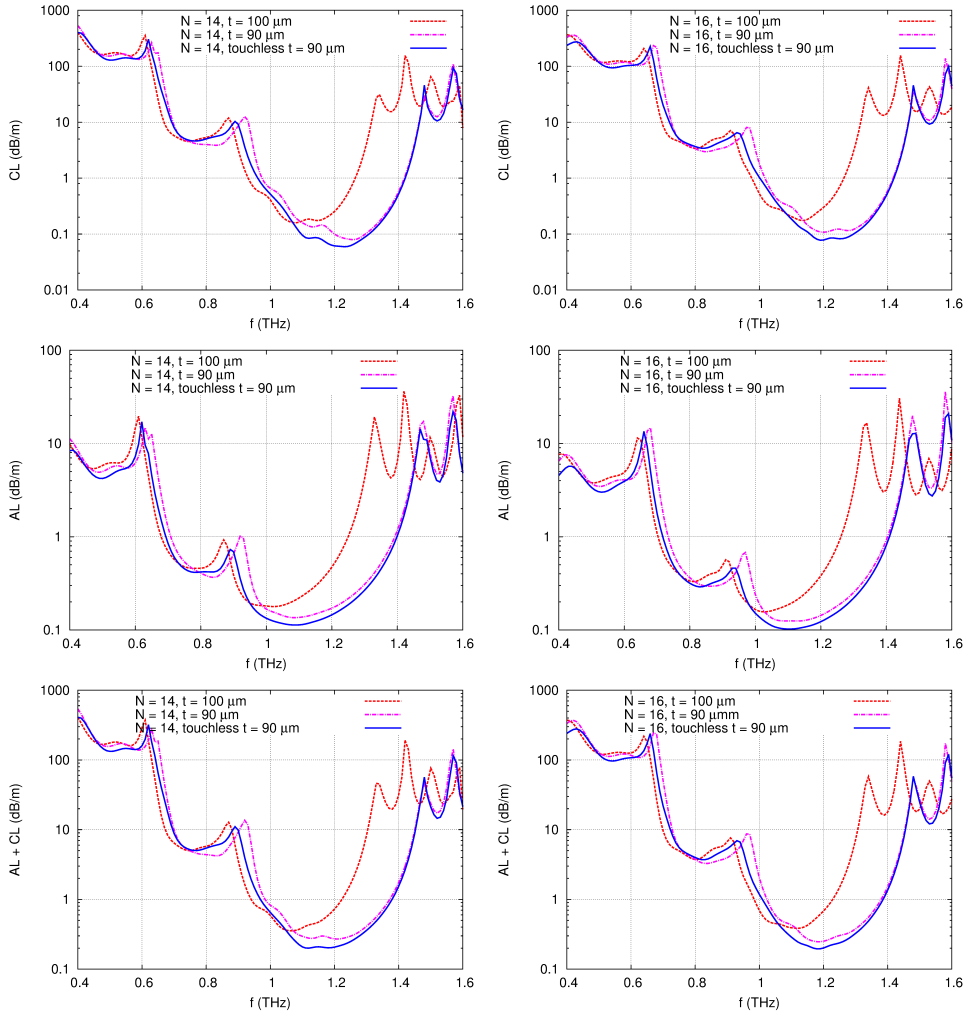

Figure 4.23: Solid line is CTLF with touchless cladding tubes for $N = 14$ (left) and $N = 16$ (right). Top: Confinement loss, Middle: Absorption loss, and Bottom: Total Loss. CTLF with tube thickness $t = 100$ μm in dashed line, $t = 90$ μm in dash-dot line.

of local peak reduction, but the gain of transmission band for 20 GHz in the lower frequency (from 0.99 THz of dash-dot line to 0.97 THz solid line). The bandwidth obtained is around 400 GHz range from 0.97 THz to 1.37 THz using the touchless cladding tubes fiber design. The minimum loss achieved is 0.20 dB/m (at 1.12 THz in solid line) which is lower than 0.27 dB/m (at 1.21 THz in dash-dot line). The achievement of bandwidth is around one and a half greater than the bandwidth obtained of CTLF with t = 100 μm with lower minimum loss, for example 0.20 dB/m compared with 0.35 dB/m at 1.06 THz of CTLF with t = 100 μm.

Conclusion

The main motivation of the research activities is great design flexibility of Photonic Crystal Fibers with the combination of large choice of single dielectric material provides a wide potential applications in different areas related with the working frequencies. The first interested application is the demanding application in high power fiber lasers which has attracted the industries for their efficiency, beam quality, and easy thermal management. Here the applications are mainly working in infrared regions. Beyond IR-region, THz technologies is very interesting for high resolution imaging both for industrial and biological application. But, in this less-explored frequency, the development of fibers with low loss, broad transmission band and high free space coupling efficiency is still a hot and key issue. The challenge in waveguide development in THz frequencies is poor characteristics of both metal and dielectrics in this frequency region. PCF design explored during the PhD activities are Large Pitch Fibers (LPF), Symmetry-free PCF (SF-PCF), and Circular Tube Lattice Fiber (CTLF). The first two kinds of PCFs are suitable for high power fiber laser applications in IR regions while the latter is applicable for low-loss THz waveguiding due to the exploitation of hollow-core PCF concept and low-loss dielectric material in THz frequency. A full-vector modal solver based on the finite-element method has been used for a whole analysis of the fibers under study during the PhD program.

Large Pitch Fibers show good delocalization properties useful for high power fiber laser application when the core is formed by removing the central hole. Forming the core by removing of 7 air-holes, a larger modal area is obtained but the first higher order mode is more confined in the core. Removing the air-cladding has been

highlighted that every modes, including the fundamental mode, have high losses. The double cladding large mode area PCF of $\sim$80 μm-core between LPF and the design of reduced cladding symmetry called by Symmetry-free PCF (SF-PCF) have been investigated, aiming to obtain robust Single Mode guiding even at high heat load values, such as those generated during operation of high-power Tm-doped fiber lasers. A full-vector modal solver based on the finite-element method with integrated thermal model to calculate temperature-induced refractive index change has been applied to analyze the effects of the main fiber design parameters on the modal discrimination for different heating conditions. The results have shown that the SF-PCF is capable of providing efficient suppression of the HOMs, with maximum overlap difference between the FM and the most detrimental HOM larger than 0.5, even when relevant heat load is assumed. SM propagation with A_{eff} larger than 2500 μm^2 has been demonstrated at heat load of 340 W/m. This result shows that SF-PCF provides the better modal discrimination at the highest possible power for single-mode operation of high power fiber laser than LPF. The latter shows a lower modal discrimination of around 0.3 at the mid-infrared (around 2 μm) in the same heat load of 340 W/m.

Scaling laws of the CTLFs losses have been numerically investigated with the purpose to obtain design guidelines for small and flexible low loss waveguides. The dependence of the confinement loss on core size, and working frequency are obtained. Results have shown confinement loss exhibits a stronger dependence of core size and frequency with respect to other kind of hollow core fibers such as Tube, Bragg, and Kagome fibers since it scale as the 4.5 power of both frequency and core radius. The dielectric overlap dependence is weaker than confinement loss both on core radius and on frequency. Dielectric overlap scales with the factor of 3 and 2 for the core radius and frequency, respectively. In AL the frequency dependence is further reduced because of usually the absorption coefficient of dielectric materials α_d increases with frequency. CTLF with fiber diameter of 5 mm, tube thickness 100 μm and number of tubes N = 16 provides a remarkable transmission band of about an octave in THz frequency, ranging from 0.7 THz to 1.3 THz considered only in the first Transmission Windows when the allowable loss is set to 10 dB/m. By reducing the reference loss value as low as 1 dB/m the maximum band of 280 GHz is obtained with N = 14,

ranging from 0.94 THz to 1.22 THz. Optimized fiber designs with touchless cladding tubes, one and half times of the bandwidth have been obtained around 400 GHz range from 0.97 THz to 1.37 THz with lower minimum loss of 0.20 dB/m, compared with previous 0.35 dB/m of CTLF with $t = 100\ \mu$m.

Bibliography

[1] M. Masruri, L. Vincetti, B. Debord, M. Alharbi, T. Bradley, C. Fourcade-Dutin, Y.Y. Wang, F. Gerome, and F. Benabid. Arc curvature effect on confinement loss in hypocycloid hollow core kagome fibers. In *Proceedings of the XX RiNEm*, pages 489–492. Societa Italiana di Elettromagnetismo, 2014.

[2] V. Setti, L. Vincetti, and A. Argyros. Flexible tube lattice fibers for terahertz applications. *Opt. Express*, 21(3):3388–3399, Feb 2013. URL: `http://www.opticsexpress.org/abstract.cfm?URI=oe-21-3-3388`, `doi:10.1364/OE.21.003388`.

[3] Anton N. Kolyadin, Alexey F. Kosolapov, Andrey D. Pryamikov, Alexander S. Biriukov, Victor G. Plotnichenko, and Evgeny M. Dianov. Light transmission in negative curvature hollow core fiber in extremely high material loss region. *Opt. Express*, 21(8):9514–9519, Apr 2013. URL: `http://www.opticsexpress.org/abstract.cfm?URI=oe-21-8-9514`, `doi:10.1364/OE.21.009514`.

[4] Jens Limpert, Fabian Stutzki, Florian Jansen, Hans-Jürgen Otto, Tino Eidam, Cesar Jauregui, and Andreas Tünnermann. Yb-doped large-pitch fibres: effective single-mode operation based on higher-order mode delocalisation. *Light Sci Appl*, 1(e8):1–5, Apr 2012. URL: `http://dx.doi.org/10.1038/lsa.2012.8`, `doi:10.1038/lsa.2012.8`.

[5] Philip Russell. History and future of photonic crystal fibers. In *Optical Fiber Communication Conference and National Fiber Optic Engineers Conference*,

page OTuC1. Optical Society of America, 2009. URL: http://www.opticsinfobase.org/abstract.cfm?URI=OFC-2009-OTuC1, doi:10.1364/OFC.2009.OTuC1.

[6] T. A. Birks, J. C. Knight, and P. St.J. Russell. Endlessly single-mode photonic crystal fiber. *Opt. Lett.*, 22(13):961–963, Jul 1997. URL: http://ol.osa.org/abstract.cfm?URI=ol-22-13-961, doi:10.1364/OL.22.000961.

[7] William Reeves, J. Knight, P. Russell, and P. Roberts. Demonstration of ultra-flattened dispersion in photonic crystal fibers. *Opt. Express*, 10(14):609–613, Jul 2002. URL: http://www.opticsexpress.org/abstract.cfm?URI=oe-10-14-609, doi:10.1364/OE.10.000609.

[8] N. G. R. Broderick, T. M. Monro, P. J. Bennett, and D. J. Richardson. Nonlinearity in holey optical fibers: measurement and future opportunities. *Opt. Lett.*, 24(20):1395–1397, Oct 1999. URL: http://ol.osa.org/abstract.cfm?URI=ol-24-20-1395, doi:10.1364/OL.24.001395.

[9] A. Ortigosa-Blanch, J. C. Knight, W. J. Wadsworth, J. Arriaga, B. J. Mangan, T. A. Birks, and P. St. J. Russell. Highly birefringent photonic crystal fibers. *Opt. Lett.*, 25(18):1325–1327, Sep 2000. URL: http://ol.osa.org/abstract.cfm?URI=ol-25-18-1325, doi:10.1364/OL.25.001325.

[10] J.C. Knight, T.A. Birks, R.F. Cregan, P.S.J. Russell, and J.P. de Sandro. Large mode area photonic crystal fibre. *Electronics Letters*, 34(13):1347–1348, Jun 1998. doi:10.1049/el:19980965.

[11] Florian Jansen, Martin Baumgartl, Hans-Jürgen Otto, Cesar Jauregui, Jens Limpert, and Andreas Tünnermann. Influence of index depressions in active large pitch fibers. In *Conference on Lasers and Electro-Optics 2010*, page CWC6. Optical Society of America,

2010. URL: http://www.opticsinfobase.org/abstract.cfm?URI=CLEO-2010-CWC6, doi:10.1364/CLEO.2010.CWC6.

[12] N. M. Litchinitser, A. K. Abeeluck, C. Headley, and B. J. Eggleton. Antiresonant reflecting photonic crystal optical waveguides. *Opt. Lett.*, 27(18):1592–1594, Sep 2002. URL: http://ol.osa.org/abstract.cfm?URI=ol-27-18-1592, doi:10.1364/OL.27.001592.

[13] P. J. Roberts, F. Couny, H. Sabert, B. J. Mangan, D. P. Williams, L. Farr, M. W. Mason, A. Tomlinson, T. A. Birks, J. C. Knight, and P. St.J. Russell. Ultimate low loss of hollow-core photonic crystal fibres. *Opt. Express*, 13(1):236–244, Jan 2005. URL: http://www.opticsexpress.org/abstract.cfm?URI=oe-13-1-236, doi:10.1364/OPEX.13.000236.

[14] J.S. Melinger, N. Laman, and D. Grischkowsky. The underlying terahertz vibrational spectrum of explosives solids. *Applied Physics Letters*, 93(1):011102–011102–3, Jul 2008. doi:10.1063/1.2949068.

[15] Takashi Yasuda, Yoichi Kawada, Haruyoshi Toyoda, and Hironori Takahashi. Terahertz movie of internal transmission imaging. *Opt. Express*, 15(23):15583–15588, Nov 2007. URL: http://www.opticsexpress.org/abstract.cfm?URI=oe-15-23-15583, doi:10.1364/OE.15.015583.

[16] Wai Lam Chan, Jason Deibel, and Daniel M Mittleman. Imaging with terahertz radiation. *Reports on Progress in Physics*, 70:1325–1379, Jul 2007.

[17] Masayoshi Tonouchi. Cutting-edge terahertz technology. *Nat. Photon*, 1:97–105, Feb 2007. URL: http://dx.doi.org/10.1038/nphoton.2007.3.

[18] Rudeger Kohler, Alessandro Tredicucci, Fabio Beltram, Harvey E. Beere, Edmund H. Linfield, A. Giles Davies, David A. Ritchie, Rita C. Iotti, and Fausto Rossi. Terahertz semiconductor heterostructure laser. *Nature*, 417:156–159, May 2002. URL: http://dx.doi.org/10.1038/417156a.

[19] R. Mendis and D. Grischkowsky. Plastic ribbon thz waveguides. *Journal of Applied Physics*, 88(7):4449–4451, 2000. URL: http://scitation.aip.org/content/aip/journal/jap/88/7/10.1063/1.1310179, doi:http://dx.doi.org/10.1063/1.1310179.

[20] S. P. Jamison, R. W. McGowan, and D. Grischkowsky. Single-mode waveguide propagation and reshaping of sub-ps terahertz pulses in sapphire fibers. *Applied Physics Letters*, 76(15):1987–1989, 2000. URL: http://scitation.aip.org/content/aip/journal/apl/76/15/10.1063/1.126231, doi:http://dx.doi.org/10.1063/1.126231.

[21] Li-Jin Chen, Hung-Wen Chen, Tzeng-Fu Kao, Ja-Yu Lu, and Chi-Kuang Sun. Low-loss subwavelength plastic fiber for terahertz waveguiding. *Opt. Lett.*, 31(3):308–310, Feb 2006. URL: http://ol.osa.org/abstract.cfm?URI=ol-31-3-308, doi:10.1364/OL.31.000308.

[22] Sébastien Février, Benoît Beaudou, and Pierre Viale. Understanding origin of loss in large pitch hollow-core photonic crystal fibers and their design simplification. *Opt. Express*, 18(5):5142–5150, Mar 2010. URL: http://www.opticsexpress.org/abstract.cfm?URI=oe-18-5-5142, doi:10.1364/OE.18.005142.

[23] Florian Jansen, Fabian Stutzki, Hans-Jürgen Otto, Martin Baumgartl, Cesar Jauregui, Jens Limpert, and Andreas Tünnermann. The influence of index-depressions in core-pumped yb-doped large pitch fibers. *Opt. Express*, 18(26):26834–26842, Dec 2010. URL: http://www.opticsexpress.org/abstract.cfm?URI=oe-18-26-26834, doi:10.1364/OE.18.026834.

[24] Philip Russell. Photonic crystal fibers. *Appl. Physics*, 299:358–362, Jan 2013. doi:10.1126/science.1079280.

[25] J.P. Webb. Hierarchal vector basis functions of arbitrary order for triangular and tetrahedral finite elements. *Antennas and Propagation, IEEE Transactions on*, 47(8):1244–1253, Aug 1999. doi:10.1109/8.791939.

[26] A. Cucinotta, G. Pelosi, S. Selleri, L. Vincetti, and M. Zoboli. Perfectly matched anisotropic layers for optical waveguide analysis through the finite-element beam-propagation method. *Microwave and Optical Technology Letters*, 23(2):67–69, 1999. URL: http://dx.doi.org/10.1002/(SICI)1098-2760(19991020)23:2<67::AID-MOP1>3.0.CO;2-V, doi:10.1002/(SICI)1098-2760(19991020)23:2<67::AID-MOP1>3.0.CO;2-V.

[27] Carlo Molardi, Masruri Masruri, Enrico Coscelli, Federica Poli, Annamaria Cucinotta, and Stefano Selleri. Fem solver optimization for pcf design. In *Proceedings of the XIX RiNEm*, pages 517–520. Societa Italiana di Elettromagnetismo, 2012.

[28] Enrico Coscelli, Federica Poli, Thomas T. Alkeskjold, Davide Passaro, Annamaria Cucinotta, Lasse Leick, Jes Broeng, and Stefano Selleri. Single-mode analysis of yb-doped double-cladding distributed spectral filtering photonic crystal fibers. *Opt. Express*, 18(26):27197–27204, Dec 2010. URL: http://www.opticsexpress.org/abstract.cfm?URI=oe-18-26-27197, doi:10.1364/OE.18.027197.

[29] Romain Dauliat, Dmitry Gaponov, Aurélien Benoit, François Salin, Kay Schuster, Raphaël Jamier, and Philippe Roy. Inner cladding microstructuration based on symmetry reduction for improvement of singlemode robustness in vlma fiber. *Opt. Express*, 21(16):18927–18936, Aug 2013. URL: http://www.opticsexpress.org/abstract.cfm?URI=oe-21-16-18927, doi:10.1364/OE.21.018927.

[30] Mette Marie Jørgensen, Sidsel Rübner Petersen, Marko Laurila, Jesper Lægsgaard, and Thomas Tanggaard Alkeskjold. Optimizing single mode robustness of the distributed modal filtering rod fiber amplifier. *Opt. Express*,

20(7):7263–7273, Mar 2012. URL: http://www.opticsexpress.org/abstract.cfm?URI=oe-20-7-7263, doi:10.1364/OE.20.007263.

[31] Stuart D. Jackson. Towards high-power mid-infrared emission from a fibre laser. *Nature Photonics*, 6:423–431, Jun 2012. URL: http://dx.doi.org/10.1038/nphoton.2012.149, doi:10.1038/nphoton.2012.149.

[32] V. Dominic, S. MacCormack, R. Waarts, S. Sanders, S. Bicknese, R. Dohle, E. Wolak, P.S. Yeh, and E. Zucker. 110 w fiber laser. In *Lasers and Electro-Optics, 1999. CLEO '99. Summaries of Papers Presented at the Conference on*, pages CPD11/1–CPD11/2, May 1999. doi:10.1109/CLEO.1999.834612.

[33] Y. Jeong, J.K. Sahu, D.N. Payne, and J. Nilsson. Ytterbium-doped large-core fibre laser with 1 kw of continuous-wave output power. *Electronics Letters*, 40(8):470–472, April 2004. doi:10.1049/el:20040298.

[34] Liang Dong, Hugh A. Mckay, Andrius Marcinkevicius, Libin Fu, Jun Li, Brian K. Thomas, and Martin E. Fermann. Extending effective area of fundamental mode in optical fibers. *J. Lightwave Technol.*, 27(11):1565–1570, Jun 2009. URL: http://jlt.osa.org/abstract.cfm?URI=jlt-27-11-1565.

[35] Tino Eidam, Jan Rothhardt, Fabian Stutzki, Florian Jansen, Steffen Hädrich, Henning Carstens, Cesar Jauregui, Jens Limpert, and Andreas Tünnermann. Fiber chirped-pulse amplification system emitting 3.8 gw peak power. *Opt. Express*, 19(1):255–260, Jan 2011. URL: http://www.opticsexpress.org/abstract.cfm?URI=oe-19-1-255, doi:10.1364/OE.19.000255.

[36] Norbert Modsching, Pankaj Kadwani, R. Andrew Sims, Lasse Leick, Jes Broeng, Lawrence Shah, and Martin Richardson. Lasing in thulium-doped polarizing photonic crystal fiber. *Opt. Lett.*, 36(19):3873–

3875, Oct 2011. URL: http://ol.osa.org/abstract.cfm?URI=ol-36-19-3873, doi:10.1364/OL.36.003873.

[37] Christian Gaida, Pankaj Kadwani, Lasse Leick, Jes Broeng, Lawrence Shah, and Martin Richardson. Cw-lasing and amplification in tm3+-doped photonic crystal fiber rod. *Opt. Lett.*, 37(21):4513–4515, Nov 2012. URL: http://ol.osa.org/abstract.cfm?URI=ol-37-21-4513, doi:10.1364/OL.37.004513.

[38] D.C. Brown and H.J. Hoffman. Thermal, stress, and thermo-optic effects in high average power double-clad silica fiber lasers. *Quantum Electronics, IEEE Journal of*, 37(2):207–217, Feb 2001. doi:10.1109/3.903070.

[39] Stuart D. Jackson. Cross relaxation and energy transfer upconversion processes relevant to the functioning of 2 μm tm3+-doped silica fibre lasers. *Optics Communications*, 230(1-3):197 – 203, 2004. URL: http://www.sciencedirect.com/science/article/pii/S0030401803022612, doi:http://dx.doi.org/10.1016/j.optcom.2003.11.045.

[40] Fabian Stutzki, Florian Jansen, Cesar Jauregui, Jens Limpert, and Andreas Tünnermann. Non-hexagonal large-pitch fibers for enhanced mode discrimination. *Opt. Express*, 19(13):12081–12086, Jun 2011. URL: http://www.opticsexpress.org/abstract.cfm?URI=oe-19-13-12081, doi:10.1364/OE.19.012081.

[41] Dmitry Gaponov, Aurelien Benoit, Francois Salin, Kay Schuster, Raphael Jamier, and Philippe Roy. Inner cladding microstructuration based on symmetry reduction for improvement of singlemode robustness in vlma fiber. *Opt. Express*, 21(16):1094–4087, Oct 2013. doi:10.1364/OE.21.018927.

[42] F. Poli, A. Cucinotta, and S. Selleri. *Photonic Crystal Fibers. Properties and Applications*. Springer Series in Material Science, Dordrecht, 2007.

[43] E. Coscelli, F. Poli, T.T. Alkeskjold, M.M. Jorgensen, L. Leick, J. Broeng, A. Cucinotta, and S. Selleri. Thermal effects on the single-mode regime of distributed modal filtering rod fiber. *Lightwave Technology, Journal of*, 30(22):3494–3499, Nov 2012. doi:10.1109/JLT.2012.2222350.

[44] Florian Jansen, Fabian Stutzki, Cesar Jauregui, Jens Limpert, and Andreas Tünnermann. High-power very large mode-area thulium-doped fiber laser. *Opt. Lett.*, 37(21):4546–4548, Nov 2012. URL: http://ol.osa.org/abstract.cfm?URI=ol-37-21-4546, doi:10.1364/OL.37.004546.

[45] Mette Marie Johansen, Kristian Rymann Hansen, Marko Laurila, Thomas Tanggaard Alkeskjold, and Jesper Lægsgaard. Estimating modal instability threshold for photonic crystal rod fiber amplifiers. *Opt. Express*, 21(13):15409–15417, Jul 2013. URL: http://www.opticsexpress.org/abstract.cfm?URI=oe-21-13-15409, doi:10.1364/OE.21.015409.

[46] Benabid F, Knight JC, Antonopoulos G, and Russel PS. Stimulated raman scattering in hydrogen-filled hollow-core photonic crystal fiber. *Science*, 298(5592):399–402, Oct 2002. doi:10.1126/science.1076408.

[47] Jonathan Shephard, J. Jones, D. Hand, G. Bouwmans, J. Knight, P. Russell, and B. Mangan. High energy nanosecond laser pulses delivered single-mode through hollow-core pbg fibers. *Opt. Express*, 12(4):717–723, Feb 2004. URL: http://www.opticsexpress.org/abstract.cfm?URI=oe-12-4-717, doi:10.1364/OPEX.12.000717.

[48] Andrey D. Pryamikov, Alexander S. Biriukov, Alexey F. Kosolapov, Victor G. Plotnichenko, Sergei L. Semjonov, and Evgeny M. Dianov. Demonstration of a waveguide regime for a silica hollow - core microstructured optical fiber with a negative curvature of the core boundary in the spectral region > 3.5 μm. *Opt. Express*, 19(2):1441–1448, Jan 2011. URL: http://www.opticsexpress.org/abstract.cfm?URI=oe-19-2-1441, doi:10.1364/OE.19.001441.

[49] Luca Vincetti. Numerical analysis of plastic hollow core microstructured fiber for terahertz applications. *Optical Fiber Technol.*, 15(4):398–401, Aug 2009. doi:doi:10.1016/j.yofte.2009.05.002.

[50] Luca Vincetti and Valerio Setti. Waveguiding mechanism in tube lattice fibers. *Opt. Express*, 18(22):23133–23146, Oct 2010. URL: http://www.opticsexpress.org/abstract.cfm?URI=oe-18-22-23133, doi:10.1364/OE.18.023133.

[51] Alexey F. Kosolapov, Andrey D. Pryamikov, Alexander S. Biriukov, Vladimir S. Shiryaev, Maxim S. Astapovich, Gennady E. Snopatin, Victor G. Plotnichenko, Mikhail F. Churbanov, and Evgeny M. Dianov. Demonstration of co2-laser power delivery through chalcogenide-glass fiber with negative-curvature hollow core. *Opt. Express*, 19(25):25723–25728, Dec 2011. URL: http://www.opticsexpress.org/abstract.cfm?URI=oe-19-25-25723, doi:10.1364/OE.19.025723.

[52] Walter Belardi and Jonathan C. Knight. Hollow antiresonant fibers with low bending loss. *Opt. Express*, 22(8):10091–10096, Apr 2014. URL: http://www.opticsexpress.org/abstract.cfm?URI=oe-22-8-10091, doi:10.1364/OE.22.010091.

[53] Masruri Masruri, Luca Vincetti, Carlo Molardi, Enrico Coscelli, Annamaria Cucinotta, and Stefano Selleri. Confinement loss scaling law analysis in tube lattice fibers for terahertz applications. In *Proc. SPIE, Terahertz, RF, Millimeter, and Submillimeter-Wave Technology and Applications VII, 89850F*, volume 8985, pages 89850F–1–89850F–6, March 2014. doi:10.1117/12.2039097.

[54] E. A. J. Marcatili and R. A. Schmeltzer. Hollow metallic and dielectric waveguides for long distance optical transmission and lasers. *Bell System Technical Journal*, 43(6):1783–1809, 1964. doi:10.1002/j.1538-7305.1964.tb04108.x.

[55] A. B. Manenkov. Quasi optics of waveguides with selective reflecting dielectric walls. *Proc. of the Fifth Colloquim on Microwave Communications*, Jun 1974.

[56] D.S. Wu, A. Argyros, and S.G. Leon-Saval. Reducing the size of hollow terahertz waveguides. *Lightwave Technology, Journal of*, 29(1):97–103, Jan 2011. doi:10.1109/JLT.2010.2093121.

[57] Shaghik Atakaramians, Shahraam Afshar V., Bernd M. Fischer, Derek Abbott, and Tanya M. Monro. Porous fibers: a novel approach to low loss thz waveguides. *Opt. Express*, 16(12):8845–8854, Jun 2008. URL: http://www.opticsexpress.org/abstract.cfm?URI=oe-16-12-8845, doi:10.1364/OE.16.008845.

[58] M. Masruri, A. Cucinotta, S. Selleri, and L. Vincetti. Circular tube lattice fibers for terahertz applications. In *Photonics Technologies, 2014 Fotonica AEIT Italian Conference on*, pages 1–4, May 2014. doi:10.1109/Fotonica.2014.6843860.

[59] Walter Belardi and Jonathan C. Knight. Negative curvature fibers with reduced leakage loss. In *Optical Fiber Communication Conference*, page Th2A.45. Optical Society of America, 2014. URL: http://www.opticsinfobase.org/abstract.cfm?URI=OFC-2014-Th2A.45, doi:10.1364/OFC.2014.Th2A.45.

[60] Jessienta Anthony, Rainer Leonhardt, Sergio G. Leon-Saval, and Alexander Argyros. Thz propagation in kagome hollow-core microstructured fibers. *Opt. Express*, 19(19):18470–18478, Sep 2011. URL: http://www.opticsexpress.org/abstract.cfm?URI=oe-19-19-18470, doi:10.1364/OE.19.018470.

[61] O. Mitrofanov, R. James, F.A. Fernandez, T.K. Mavrogordatos, and J.A. Harrington. Reducing transmission losses in hollow thz waveguides. *Terahertz Science and Technology, IEEE Transactions on*, 1(1):124–132, Sept 2011. doi:10.1109/TTHZ.2011.2159547.

[62] Luca Vincetti. Single-mode propagation in triangular tube lattice hollow-core terahertz fibers. *Optics Communications*, 283(6):979–984, March 2010. doi:doi:10.1016/j.optcom.2009.11.025.

[63] Jessienta Anthony, Rainer Leonhardt, Alexander Argyros, and Maryanne C. J. Large. Characterization of a microstructured zeonex terahertz fiber. *J. Opt. Soc. Am. B*, 28(5):1013–1018, May 2011. URL: http://josab.osa.org/abstract.cfm?URI=josab-28-5-1013, doi:10.1364/JOSAB.28.001013.

Aknowledgments

I would like to express my special appreciation and sincere thanks to my advisor Professor Stefano Selleri, you have been a tremendous mentor for me. I would like to thank you for encouraging me from the beginning of my joining to your research group. Your advice, patience, and support on my PhD study from the beginning have been priceless, including to obtain the scholarship which was not so easy.

I would also like to thank to Prof. Luca Vincetti, Department of Engineering "Enzo Ferrari", University of Modena and Reggio Emilia, for your research collaboration during my second and third year of my PhD study. I have learned so much from you during the activities. I would also like to thank to Prof.ssa Annamaria Cucinotta for discussion, help, and encouragement during my study. I would like to sincerely thank to Prof. Marco Locatelli as the PhD coordinator and my professors in the members of the Commission for the supports during my PhD study.

I will also like to acknowledge a number of my friends and colleagues, without whom, this experience would have been incomplete. Firstly, I want to thank to Carlo Molardi who has helped me in the first year of my PhD study. Enrico Coscelli, thank you for collaboration in some PhD activities. Alessandro Candiani and Michele Sozzi who gived me another experience to enrich me, beyond my PhD topics in laser cutting and biosensor. Federica Poli for the special lecture and Lorenzo Rosa for the discussion. Special thanks to Maurizio Mottola for continuous support in preparing and maintaining the simulation server.

I would like to thank my parents who always support me with love and encouragement. This PhD study is their dream. To my beloved wife, daughter and son who

always beside me in completing my PhD study. Completing the PhD together with beloved family was my dream after being so long without them during my master degree.

Finally, I'm thankful for all of my close friends who have supported me, without I mention the name one by one.